Methods and requirements for accurate localisation of sensors in on-scalp magnetoencephalography

Rasmus Zetter

School of Electrical Engineering

Thesis submitted for examination for the degree of Master of Science in Technology.

Espoo 28.9.2016

Thesis supervisor and advisor:

Prof. Lauri Parkkonen

Aalto University
School of Electrical
Engineering

Author: Rasmus Zetter

Title: Methods and requirements for accurate localisation of sensors in on-scalp magnetoencephalography

Date: 28.9.2016 Language: English Number of pages: 7+57

Aalto University School of Science

Department of Neuroscience and Biomedical Engineering

Professorship: Biomedical Engineering

Supervisor and advisor: Prof. Lauri Parkkonen

Magnetoencephalography (MEG) is a noninvasive functional neuroimaging method which is used both in neuroscientific research and clinical medicine. Current state-of-the-art MEG systems require cryogenic cooling as well as thermal insulation between the sensors and the head of subjects, leading to lower sensitivity due to the relatively large spatial separation.

Recently, a new type of sensor has been developed that does not require cryogenic temperatures to operate and can thus be placed much closer to the scalp of subjects. In such an on-scalp MEG system, the sensors of the array could be freely moveable in relation to each other as to conform to the head shape and size of individual subjects. To properly estimate the location and extent of neural sources within the brain, one needs to accurately know the position of all sensors in relation to the head. In on-scalp MEG systems this seemingly mundane issue becomes important, as all sensors must be localised individually. Large errors in the sensor positions may result in considerable errors in source estimates.

In this thesis, different sensor localisation methods to be used in co-registration of MEG data with structural magnetic resonance images were examined, and the performance requirements for such methods were determined through the use of simulations. We found that the maximum acceptable root-mean-square sensor position error is ~ 3 mm, which is achievable for most localisation methods examined. Thus the choice of method depends less on the localisation accuracy and more on other parameters such as ease of use, cost and commercial availability.

Keywords: magnetoencephalography, optically-pumped magnetometer, co-registration, simulation

AALTO-UNIVERSITETET
HÖGSKOLAN FÖR ELEKTROTEKNIK

SAMMANDRAG AV
DIPLOMARBETET

Författare: Rasmus Zetter

Titel: Metoder och krav för noggrann lokalisering av sensorer i *on-scalp* magnetoencefalografi

Datum: 28.9.2016 Språk: Engelska Sidantal: 7+57

Högskolan för teknikvetenskaper

Institutionen för neurovetenskap och biomedicinsk teknik

Professur: Biomedicinsk teknik

Övervakare och handledare: Prof. Lauri Parkkonen

Magnetoencefalografi (MEG) är en noninvasiv metod för undersökning av hjärnfunktion. MEG används både inom neurovetenskaplig forskning och klinisk medicin. Nuvarande MEG-system kräver kryogen nedkylning och värmeisolering mellan sensorerna och försökspersonens huvud, vilket leder till nedsatt känslighet på grund av det relativt stora avståndet mellan sensorerna och hjärnan.

Nyligen har en ny typ av sensorer utvecklats som inte kräver kryogen nedkylning, och kan därmed placeras mycket närmare huvudet. I ett så kallat ön-scalpMEG-system kunde sensorerna vara fritt flyttbara i förhållande till varandra för att på bästa sätt passa försökspersonens huvudform och -storlek.

För att kunna avgöra varifrån inuti hjärnan MEG-signaler härstammar bör man veta sensorernas exakta position i förhållande till huvudet. I ett on-scalp MEG-system blir detta synligtvis triviala problem viktigt, i och med att alla sensorer måste lokaliseras enskilt. Ifall det uppstår fel i deras positioner kan detta orsaka märkbara fel i var hjärnaktiviteten som givit upphov till MEG-signalen avgörs vara.

I detta diplomarbete har olika metoder för att lokalisera sensorerna undersökts, och noggrannhetskraven för dessa metoder har fastställts genom flera olika typers simuleringar. Utgående från dessa fastställdes det maximala tolererbara kvadratiska medelvärdesfelet i sensorernas position till ~ 3 mm. Denna noggrannhetsnivå är uppnåelig för de flesta av de undersökta lokaliseringsmetoderna. Därmed bör valet av lokaliseringsmetod grunda sig på andra variabler såsom användarvänlighet, bekostnad och kommersiell tillgänglighet.

Nyckelord: Magnetoencefalografi, optiskt pumpad magnetometer, samregistrering, simulering

Preface

I would like to thank Professor Lauri Parkkonen for his guidance and the opportunity to work on the very exciting topic covered in this thesis. I would also wish to thank Matti Stenroos for his advice regarding bioelectromagnetic modelling and Joonas Iivanainen for his help in getting started as well as his advice along the way. Finally I would like to thank my friends and family who have supported me during the writing of this thesis and my studies at Aalto University.

Otaniemi, 28.9.2016

Rasmus W. M. Zetter

Contents

Operators and abbreviations

Operators

$\nabla \mathbf{A}$	gradient of $\mathbf{A}$
$\nabla \cdot \mathbf{A}$	divergence of $\mathbf{A}$
$\nabla \times \mathbf{A}$	curl of $\mathbf{A}$
$\frac{\mathrm{d}}{\mathrm{d}t}$	derivative with respect to variable t
$\frac{\partial}{\partial t}$	partial derivative with respect to variable t
$\int \phi dV$	integral of ϕ over volume V
$\int_{\mathbf{S}} \mathbf{A} \cdot d\mathbf{S}$	integral of $\mathbf{A}$ over surface $\mathbf{S}$
$\sum_{i=1}^{K}$	sum over indices i from $i = 1$ to $i = K$
$\sum_i$	sum over (all) indices i
$\mathbf{a} \cdot \mathbf{b}$	dot product of vectors $\mathbf{a}$ and $\mathbf{b}$
$tr(\mathbf{A})$	trace of $\mathbf{A}$
$\|\|\mathbf{b}\|\|$	Euclidean norm of vector $\mathbf{b}$
$\mathbf{A}^T$	transpose of matrix $\mathbf{A}$
$E[\mathbf{A}]$	expectation value of $\mathbf{A}$
$\overline{\mathbf{A}}$	mean of $\mathbf{A}$

Notation

In this thesis, the mathematical notation is such that scalars are represented by small, italic letters (e.g. b) while vectors are represented by small, bold letters (e.g. $\mathbf{b}$) and matrices are represented by capital bold letters (e.g. $\mathbf{B}$). Subscripts generally represent indices (e.g. $\mathbf{b}_i$ being the ith element of $\mathbf{b}$), while superscripts (e.g. $\mathbf{b}^{\mathrm{ref}}$) are used for other explanatory parameters.

Abbreviations

BEM	boundary element method/model
BPE	beamformer position error
CC	correlation coefficient
CSF	cerebrospinal fluid
DC-SQUID	direct current superconducting quantum interference device
ECD	equivalent current dipole
EEG	electroencephalography
EPSP	excitatory postsynaptic potential
FEM	finite element method
fMRI	functional magnetic resonance imaging
GOF	goodness-of-fit
HPI	head position indicator
IPSP	inhibitory postsynaptic potential
ISA	isolated source approach
LCMV	linearly constrained minimum-variance
MEG	magnetoencephalography
MNE	minimum-norm estimate/estimation
MR	magnetic resonance
MRI	magnetic resonance imaging
MSR	magnetically shielded room
OPM	optically-pumped magnetometer
PPE	peak position error
PSF	point-spread function
PSP	postsynaptic potential
RE	relative error
RF	radio-frequency
SD	spin-destruction
SE	spin-exchange
SERF	spin-exchange relaxation-free
SFT	superconducting flux transformer
SNR	signal-to-noise ratio
SQUID	superconducting quantum interference device

1 Introduction

Magnetoencephalography (MEG) is a non-invasive functional neuroimaging method for investigating neuronal activity inside the living human brain (Hämäläinen et al., 1993). MEG, as suggested by the name, functions by measuring the magnetic fields produced by the brain using sensors around the head. Since these biomagnetic fields are very weak, on the scale of a billionth of the Earth's geomagnetic field, exceptionally sensitive equipment is needed to measure them. In addition, one needs to attenuate environmental magnetic noise considerably. Therefore measurements are carried out in magnetically shielded rooms as well as using gradiometers and signal processing techniques to minimise noise.

To this point, the main type of magnetometer used for MEG has been the superconducting quantum interference device (SQUID). As implied by the name, this type of sensor requires the use of liquid helium to cool it down to ~4 K (−269° C) and must thus be placed within a helmet-shaped insulated container, a *dewar*. Due to this insulation the SQUIDs cannot be placed closer to the scalp than ~2 cm, and as sensitivity and spatial resolution is directly related to the distance between the brain and the sensors this results in significant loss of signal. In addition, the position of the sensors cannot be adapted to conform to the head shape of individual subjects, further increasing the sensor-scalp-separation and weakening sensitivity.

Recently optically-pumped magnetometers (OPMs) with high enough sensitivity to be used for MEG has been developed. The sensitivity of these sensors can be similar or even surpass that of SQUIDs. The major advantage of this type of sensor is that is does not require any cryogenic cooling and can thus be placed much closer to the scalp, boosting the sensitivity to neuromagnetic sources considerably. Such an *on-scalp* MEG system brings with it several practical challenges.

One of these challenges is how to accurately localise the MEG sensors with respect to the head of the subject. To be able to determine from where in the brain some measured neuromagnetic signal originated (i.e. perform so-called *source estimation*), one needs to accurately know the position of all sensors in relation to the head, and by extension to the neural sources in question. In practice, source estimates are used in conjunction with structural magnetic resonance (MR) images of the head, allowing for the visualisation of the source estimate on an image of the actual brain. For this to possible, the MEG data have to be *co-registered* with the MR image, i.e. the data from both modalities have to be transformed into a common coordinate system.

In current SQUID-based MEG systems, the sensors are rigidly mounted to the dewar, and thus only the position of the head of the subject needs to be determined. In an on-scalp MEG system where sensors are freely moveable in relation to each other, co-registration becomes more challenging and errors might be manifested in other, unexplored, ways.

In this work, different co-registration methodologies that can be applied to an on-scalp MEG system are investigated from both a practicality and performance perspective. To determine the required sensor localisation accuracy, simulations of a hypothetical OPM-based on-scalp MEG system were performed.

2 Background

The purpose of this section is to give an introduction to the subject matter reviewed in this thesis. First, the basics of MEG are covered and a perspective on the current state of MEG technology and instrumentation is given. Second, the advantages of on-scalp MEG using OPMs compared to the current SQUID-based MEG systems are discussed. Third, a variety of methods to achieve accurate co-registration in on-scalp MEG are presented and evaluated.

2.1 Magnetoencephalography

Magnetoencephalography has achieved some degree of adoption in both neuroscientific research and in clinical medicine, where it is mostly used for localisation of epileptic foci and presurgical mapping of brain function. This success is due to the high temporal resolution of MEG in combination with its relatively good spatial resolution. Current barriers to further adoption are the large costs associated with the purchase and upkeep of the equipment as well as its considerable bulk.

2.1.1 Neural basis

The human brain consists mainly of nerve cells, or *neurons*, as well as supporting cells called *glia*, which provide a variety of essential functions such as vasodilation, enforcement of ion balance, and transport of nutrients. Neurons are the actual information processing units, with an adult human brain containing ~100 billion (10^{11}) neurons with ~100 trillion (10^{14}) connections. The cell bodies of neurons are concentrated to the surface of the brain or *cortex*, called *grey matter*. The interior of the brain is mainly occupied by nerve fibres; this is called *white matter* due to its characteristic appearance.

Neurons consist of a cell body or *soma*, a tree of *dendrites* that receive input from other neurons and an *axon*, which conveys the output of the neuron to other neurons. The end of the axon and a dendrite of another neuron form a *synapse*, where signalling is performed using substances called *neurotransmitters*. All of these structures are pictured in Fig. 1. Electrical synapses also exist, although chemical signalling is the dominant form of information transfer between neurons in the nervous system.

Within the cell membrane lie *ion pumps*, which as the name implies actively move certain ion species across the membrane. Using these pumps, a transmembrane resting state voltage of approximately −70 mV (the inside of the cell is more negative than the extracellular fluid) is maintained by pumping potassium and sodium ions across the membrane.

When neurotransmitters arrive at the cell membrane of the receiving neuron in a synapse, i.e. at the post-synaptic membrane, *ion channels* in the membrane are opened, selectively letting specific ion species move passively through. Depending on the type of neurotransmitter, different ion channels will open, either raising the transmembrane voltage and thus causing an *excitatory post-synaptic potential* (EPSP) or lowering the voltage and causing an *inhibitory post-synaptic potential* (IPSP). Regardless of membrane voltage, there is no accumulation of charge within the cell, and thus when

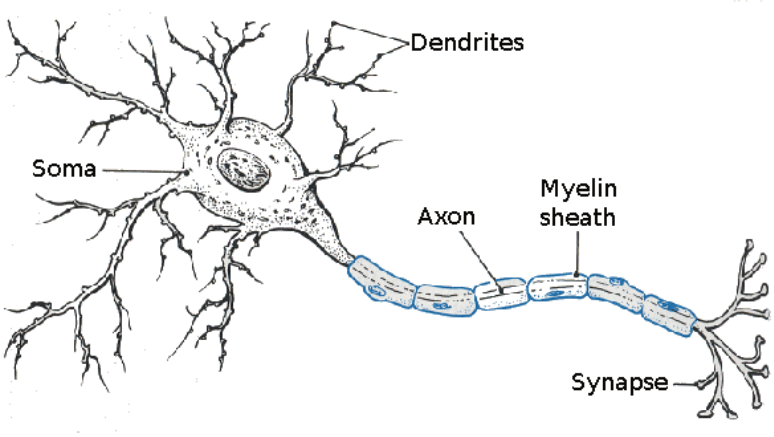

Figure 1: Illustration of a stereotypical neuron. Adapted from Carlson (1992).

there is inwards or outwards flow of ions at a synapse, be they positive or negative, there are compensating *volume ion currents* elsewhere along the cell membrane that close the electrical loop.

Post-synaptic potentials (PSPs) are relatively long-lasting (on the order of a few milliseconds to hundreds of milliseconds), and the PSPs from all inputs to the cell are summed up. If the resultant transmembrane voltage at the root of the axon by the soma, i.e. at the *axon hillock*, exceeds an activation threshold of approximately -55 mV, an *action potential* is produced. An action potential consists of a rapid change of membrane voltage due to a sudden influx of sodium ions, such that the voltage suddenly jumps to $+35$ mV and in $1-2$ milliseconds returns to the resting voltage followed by a refractory period of 1 millisecond. This voltage spike is actively propagated along the axon to the synapse without losing in amplitude, where neurotransmitters are released in response. A large part of neurons in the central nervous system have a *myelin sheath*, an electrically insulating layer, covering their axons. This feature greatly accelerates the propagation of action potentials.

The intracellular potential changes due to PSPs cause a current flow along the dendrites. Viewed from afar, this can be modelled as a current dipole producing a magnetic field. The magnetic fields measured by MEG mainly have their origin in a type of neuron in the gray matter of the brain called pyramidal neurons. These neurons can give rise to extracranial magnetic fields since their apical dendrites are all oriented perpendicularly to the surface of the cortex. Thus, the magnetic fields of nearby neurons are spatially summated. As PSPs have a long enough lifetime, temporal summation of the PSPs of neighbouring neurons also occurs. Since action potentials are so short-lived, the vast majority of the magnetic field measured by MEG stems from synchronous PSPs of tens of thousands of neurons (Murakami & Okada, 2006).

Besides temporal and spatial summation, several other factors affect the measured signal strength other than the temporally and spatially summated PSPs. First of all, signal strength is generally reduced as the spatial sensor–source separation grows. Another factor that affects the signal strength is source orientation. Due to the rather 'wrinkly' surface of the human brain (Fig. 2) the orientation of pyramidal cells will vary signifi-

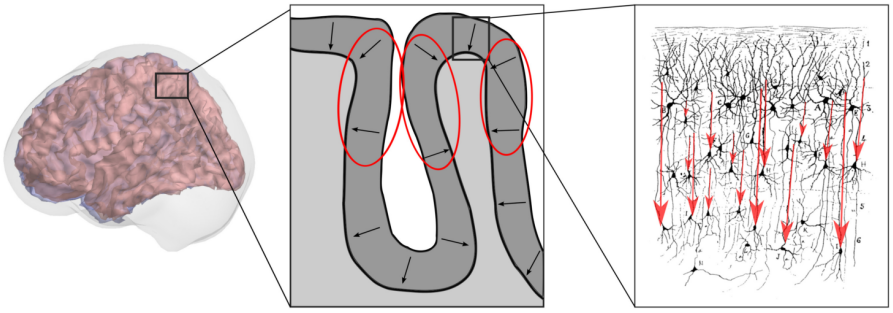

Figure 2: The main source of MEG signals is synchronous postsynaptic currents in the apical dendrites of pyramidal neurons (seen as the red arrows in the panel to the right). On a larger scale, these currents sum to larger dipolar currents in the grey matter, which are oriented orthogonally to the surface of the cortex. The sources that contribute the most to the MEG signal are circled in red in the middle panel. The panel on the right is based on a drawing by Ramón y Cajal in 1888. Reproduced from Iivanainen (2016) with permission.

cantly. At the most superficial parts of the cortex, the *gyral crowns*, the pyramidal cells are oriented radially with respect to the head, while at the *gyral walls* they are oriented tangentially. Due to the geometry of the head, MEG is mostly sensitive to tangential sources and insensitive to radial sources (Hämäläinen et al., 1993), and thus the majority of signal comes from the gyral walls. Taking into account the loss of signal along depth, the sources to which MEG is most sensitive are probably at the superficial edges of the *sulci* (i.e. the grooves in the surface of the cortex).

2.1.2 Instrumentation

SQUIDs and superconducting flux transformers

The first human MEG measurements were performed using a conventional induction coil magnetometer by Cohen (1968). In this first experiment the occipital alpha rhythm could be seen after very extensive averaging of data. Around the same time, the first SQUID was developed (Jaklevic et al., 1964) and soon after the first MEG measurements using this new technology were performed (Cohen, 1972). Ever since, the SQUID has been the sensor type used for MEG and has until recently been unchallenged as the most sensitive type of magnetometer ever developed.

SQUIDs, as the name implies, function using superconductivity, i.e. the property of some materials to lose electrical resistance as they are cooled below a critical temperature T_c. In a superconductor, electrons form *Cooper pairs*, which instead of behaving individually act coherently, following a global macroscopic wave function (Bardeen et al., 1957). Due to this phenomenon, a current running in a loop of superconducting material will never attenuate but run perpetually. This *supercurrent* will give rise to a magnetic field orthogonal to the plane of the superconducting loop. Reciprocally, in the presence of an external magnetic field a *shielding current* will be induced into the loop, giving rise to a shielding magnetic field which cancels out the external field within

the loop. Due to the phase coherence of electrons in superconductors, this magnetic field is quantized such that its flux is $n \cdot \Phi_0$, where $\Phi_0 = h/2e = 2.07$ fWb is the magnetic flux quantum (here, h is the Planck constant and e is the elementary charge). Thus, superconductors are perfect *diamagnets*; external magnetic fields (equal to or larger than Φ_0) can never be present within a superconducting loop (Hämäläinen et al., 1993).

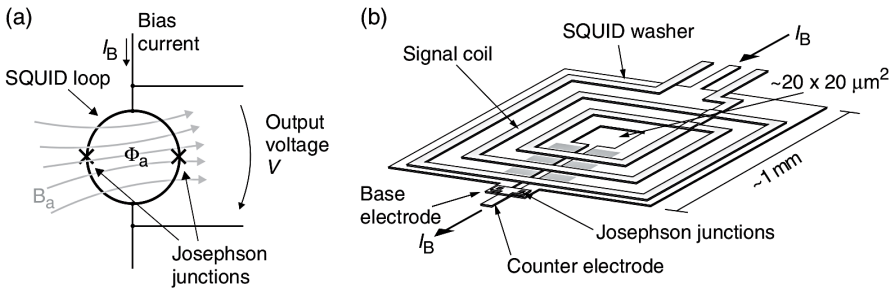

Figure 3: (a) A schematic illustration of a DC-SQUID with two Josephson junctions. The magnetic field B_a causes the magnetic flux Φ_a in the loop. (b) Realistic depiction of a modern thin-film DC-SQUID with the signal coil visible on top of the SQUID loop. Reproduced from Parkkonen (2010).

To measure an external magnetic field using a superconducting loop, in principle one could measure the current running in it. This is, however, not possible in practice. Instead, two so-called *Josephson junctions* (Josephson, 1962) are placed in the superconducting loop as in Fig. 3a, producing a so-called direct current superconducting quantum interference device, or DC-SQUID. A Josephson junction is a very thin layer of electrical insulator that the Cooper pairs of the superconductor can quantum tunnel through. The two Josephson junctions in the loop create phase interference in the wave function of the Cooper pairs (Barone & Paterno, 1982), resulting in a flux-dependent resistance, which can be measured.

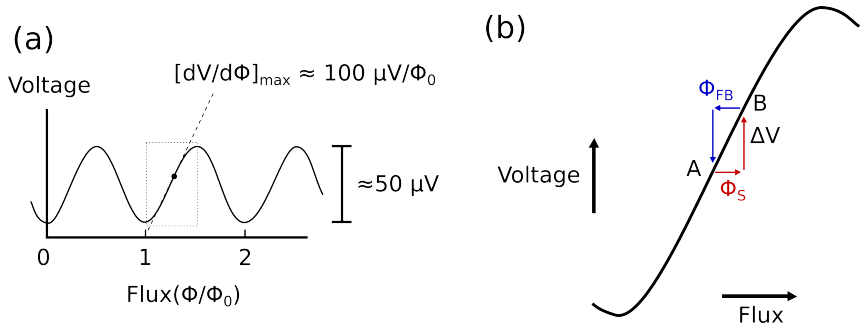

Figure 4: (a) Periodic voltage-flux-relation of SQUIDs. (b) Magnified section of (a), showing the operational principle of a flux-locked loop, where change in the signal flux Φ_S is continuously compensated by the negative feedback flux Φ_{FB}. Adapted from Lee and Kim (2014).

The resistance in a superconducting loop due to the Josephson junctions is periodically dependent on the magnetic flux. If the flux changes with $n \cdot \Phi_0$ the resistance is

unchanged (Fig. 4a), leading to ambiguous results. Thus, the dependence needs to be linearised for a SQUID to be useful for practical measurements. To this end, the SQUID is driven in a *flux-locked loop* (Fig. 4b). In this configuration, the external magnetic field in the SQUID is constantly zeroed by applying negative feedback using a feedback controller and coil, thus locking the SQUID to a certain *operating point*. Unlike the output of the SQUID, this feedback signal is linearly dependent on the measured magnetic flux. Due to this measurement set-up, SQUIDs cannot measure absolute magnetic fields but only relative field changes.

SQUIDs are typically manufactured as to be very small to minimise noise. As such, their sensitivity to magnetic fields of interest is also small due to a small flux pick-up area. To improve the sensitivity to sources of interest, *superconducting flux transformers* (SFTs) are used. An SFT consists of a large *pick-up coil* positioned as close to the brain as possible and small *signal coil* located right on top the SQUID. These two coils are connected in series, thus "concentrating" the flux from the large pick-up coil into the SQUID through the signal coil. Since the SFT is also superconducting it functions for static fields, while normal transformers do not.

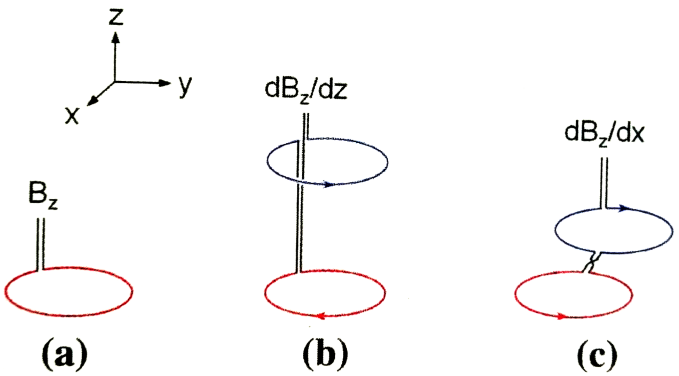

Figure 5: Pick-up coils used in SFTs. (a) magnetometer, (b) first-order axial gradiometer and (c) first-order planar gradiometer. Reproduced from Lee and Kim (2014).

Additionally, the use of SFTs allow for the design and use of different coil configurations. If the pick-up coil is a simple loop in the x-y plane, the measured quantity is the magnetic flux density B_z orthogonal to the plane of the loop, and the resultant sensor is called a *magnetometer*. However, by using different coil geometries (see Fig. 5 for examples), one can create *gradiometers*. For example, two oppositely wound coils connected in series result in a first-order gradiometer, which measures one component of the spatial derivative of the flux density. If the coils are positioned side-by-side along the x-axis the quantity measured is $\partial B_x/\partial x$; if the coils are on the same axis it is $\partial B_z/\partial z$.

The spatial sensitivity profile, or *lead field*, of a sensor is determined by the geometry of the pick-up coil. Some examples can be seen in Fig. 6. The lead field is a vector field which relates the output signal **b** of a sensor to the (neural) current sources **j** at all locations, such that

$$\mathbf{b} = \mathbf{L}\mathbf{j}. \tag{1}$$

where **j** is a vector in which every element corresponds to a unique source location. In

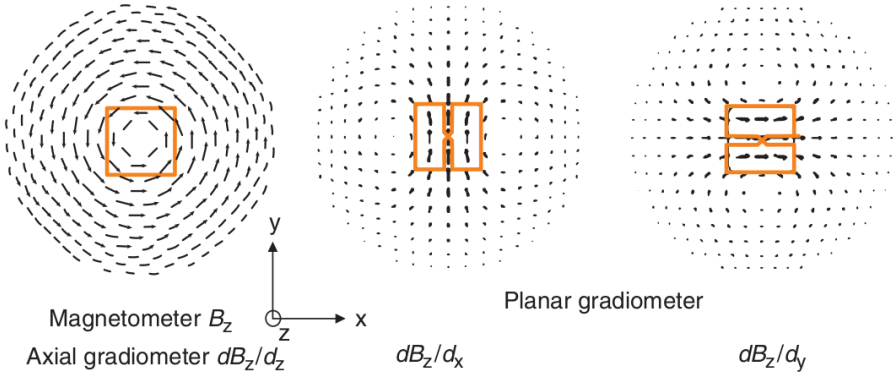

Figure 6: Two-dimensional visualisations of the sensitivity distributions of (a) a magnetometer measuring B_z, planar gradiometers measuring (b) $\partial B_z/\partial x$ and (c) $\partial B_z/\partial y$. Here the coils are rectangular instead of circular, but the same principles apply. Reproduced from Parkkonen (2010).

practice **L** is usually a matrix in which every column corresponds to the sensitivity to all sources of a sensor in a *sensor array* covering the head, and thus **b** is a vector consisting of the measured magnetic fields of every sensor in the array.

Cryogenics

As both SQUIDs and SFTs need to be superconducting to function they are immersed in liquid helium, which has a boiling temperature of 4.2 K. Both the sensors and the helium are then housed within a large insulating helmet-shaped *dewar* (Fig. 7). The dewar needs to be as thin as possible to bring the pick-up coils as close to the head as possible, and on the other hand it needs to be insulating enough to keep helium boil-off rate at acceptable levels. The dewar consists of two concentric vessels with a vacuum jacket and a radiation shield in between, and it has to be strictly non-magnetic as not to distort the measured magnetic field. In spite of this, the thermal insulation contributes to the noise level of the MEG system due to the thermal magnetic noise of the aluminium and copper used in the insulation (Lee & Kim, 2014). Despite the extreme thermal insulation, there is still some degree of heat leakage to the interior of the dewar, resulting in helium boil-off. The evaporated helium exits the dewar though an exhaust line and is either collected for reliquification or sim-

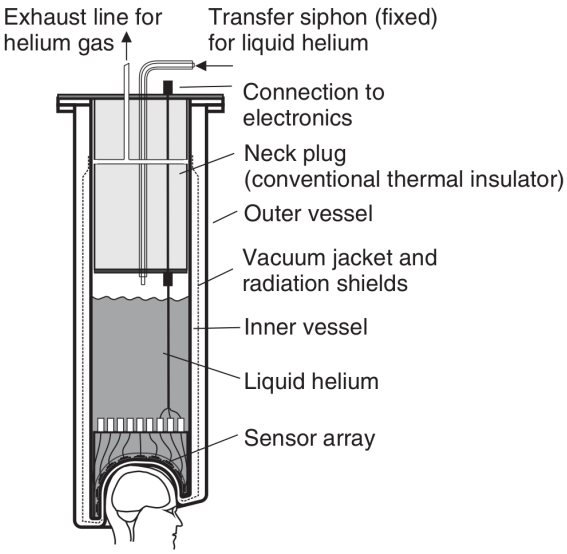

Figure 7: Schematic of a MEG probe unit within the insulating dewar. Reproduced from Parkkonen (2010).

ply vented into the atmosphere. Reliquification equipment adds additional bulk and costs to the MEG system, but as helium prices have risen these recycling systems have become more common in MEG and other superconducting equipment such as MRI. If no such equipment is used the dewar will need to be refilled with liquid helium 1–3 times a week (Parkkonen, 2010), increasing costs and adding downtime to the system. Some reliquification equipment collect the liquified helium in a separate insulated container, thus not eliminating the need for dewar refilling but still vastly reducing the amount of wasted helium.

Shielding

The most important means to avoid environmental interference, which would drown out the MEG signal and to keep the sensors within their operating range is to employ a *magnetically shielded room* (MSR). The passive shielding provided by an MSR comes down to two different factors: First, ferromagnetic shielding to attenuate low frequencies, a high-permeability material is used which provides a low-reluctance path for the interfering magnetic field along the walls of the MSR, thus reducing the interference within the MSR. To this end, a nickel-iron alloy (so-called μ-metal) with a relative permeability of > 80000 is commonly employed. Second, to shield against higher frequencies (> 10 Hz) eddy-current shielding is used in the form of a high-conductivity material, usually aluminium or copper. (Lee & Kim, 2014; Parkkonen, 2010) Practical shielded rooms employ several layers of shielding of both types in the walls to improve the total shielding factor (Fig. 8). These *multi-layer* MSRs can weigh up to 10–15 tons and thus MEG systems are usually located on ground floors or in basements where structural support can be built to withstand the load.

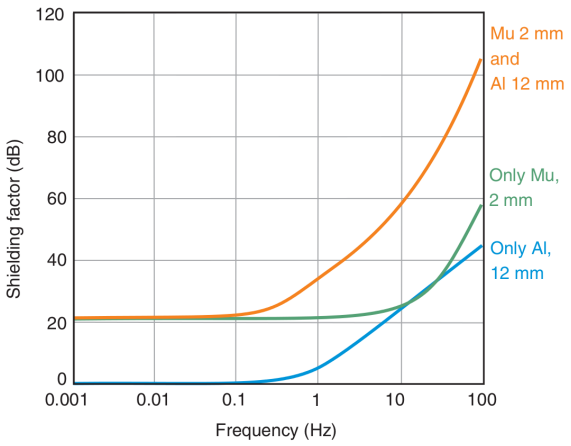

Figure 8: Estimated shielding factors as a function of frequency due to aluminium and μ-metal wall plating. Reproduced from Parkkonen (2010).

Additionally, as μ-metal is quite costly and a large amount of it is used in multi-layer MSRs, the expense of the MSR constitutes a large part of the investment to a new MEG system.

Passive MSRs can be enhanced by adding active shielding systems that work in a feedforward mode or in a negative feedback loop by constantly apply a magnetic field, which cancels the measured field using a set of coils wrapped around the MSR. When using active shielding, less extensive passive shielding can suffice. Still, active shielding is no panacea, and presents a number of technical problems on its own (Carrette et al., 2011).

The sensor array itself and the pick-up coils also have an effect on interference levels.

For example, gradiometers provide inherent suppression of interference from faraway sources, since both coils will "see" the same magnetic field and as they are oppositely wound it is cancelled out. In the case of magnetometers, one or several reference sensors placed at a small distance from the sensor array can be used for the same effect, in effect creating a synthetic gradiometer by subtracting the measured reference signal.

2.1.3 Forward modelling

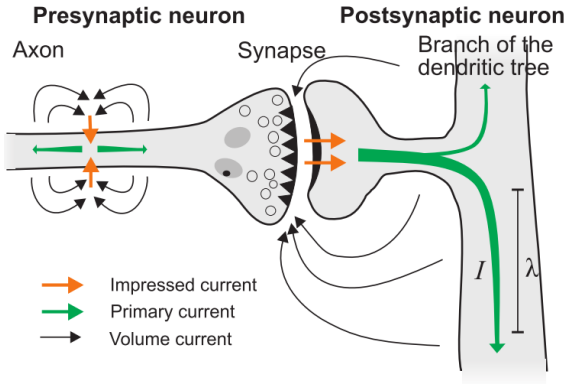

Figure 9: Cellular-level currents due to neuronal activity. Reproduced from Parkkonen (2009).

The total current density $\mathbf{J}$ of cortical sources can be said to consist of three parts on the cellular level (Fig. 9): the intracellular primary current $\mathbf{J}_p$ produced by neuronal activity, the volume current $\mathbf{J}_v = \sigma\mathbf{E}$ due to the extracellular return volume currents closing the electrical loop caused by the primary current and finally the impressed current $\mathbf{J}_i$ directly caused by the transmembrane flow of ions. The impressed currents flow for such a short distance that their resultant dipole moments have an insignificant effect on the extracranial magnetic fields, and they are thus typically neglected (Tripp, 1981). Thus the total current density can be expressed as

$$\mathbf{J} = \mathbf{J}_p + \sigma\mathbf{E} = \mathbf{J}_p - \sigma\nabla\phi \tag{2}$$

where σ is the macroscopic conductivity, without cellular-level details and ϕ is the scalar potential. Typically, the entire brain is modelled as a homogeneous conductor.

When modelling bioelectromagnetic fields, the quasistatic approximation of Maxwell's equations is typically used. In this approximation the displacement current is omitted, i.e. effects due to the finite speed of wave propagation are ignored. This means that we assume that any changes in electromagnetic sources are instantaneously seen everywhere in the fields. This assumption is seen as reasonable due to the low frequencies of the biomagnetic field and the comparatively small volume of the head. Additionally, tissue is assumed to be purely resistive, meaning that inductive and capacitive effects are ignored. Using these approximations, Maxwell's equations can be formulated as

$$\nabla \cdot \mathbf{E} = \frac{\rho}{\epsilon_0} \tag{3}$$

$$\nabla \cdot \mathbf{B} = 0 \tag{4}$$

$$\nabla \times \mathbf{E} = -\frac{\partial \mathbf{B}}{\partial t} \approx 0 \tag{5}$$

$$\nabla \times \mathbf{B} = \mu_0(\mathbf{J} + \sigma \mathbf{E}), \tag{6}$$

where $\mathbf{E}$ is the electric field and $\mathbf{B}$ is the magnetic flux density, μ_0 and ϵ_0 are the permeability and permittivity of free space, respectively, and ρ is the charge density due to the current density $\mathbf{J}$.

The magnetic field measured by a magnetometer to some known sources, which in general terms is called *the forward problem*, can be determined using the equation

$$b = \int \mathbf{L}_{j,\cdot}(\mathbf{r}) \cdot \mathbf{J}_p(\mathbf{r}) dV, \tag{7}$$

where $\mathbf{L}_{j,\cdot}$ is the lead field of that magnetometer. The lead field will depend on the conductivity $\sigma(\mathbf{r})$ of matter surrounding the magnetic sources and magnetometer as well as the geometry of the pick-up coil. Assuming that one knows the conductivity distribution and can calculate the magnetic field at the sensor locations due to any magnetic sources, the lead field is readily obtained. To obtain a complete lead field describing the sensitivity of a sensor, one typically computes the measured field caused by individually placed magnetic dipoles at each source location, oriented along each of the three axes in space.

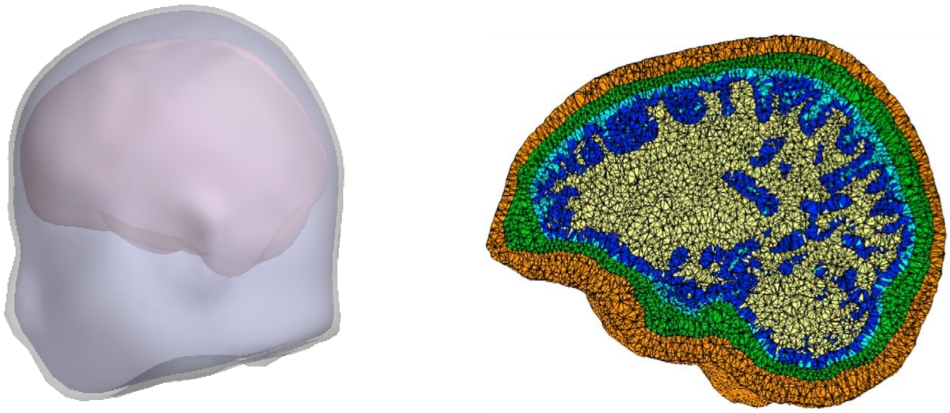

(a) (b)

Figure 10: (a) Example of BEM boundary meshes corresponding to scalp, skull and brain using realistic surfaces reconstructed from an MR image. Alternatively, volumetric meshes (b) are used when applying FEM, here illustrated with a cut-through with colour-coded tissue types with different conductivities (orange = scalp, green = skull, cyan = cerebrospinal fluid, blue = gray matter, beige = white matter). (b) Reproduced from Wolters and colleagues (2006).

In practice, the lead fields are determined numerically using the *boundary element method* (BEM), or alternatively the *finite element method* (FEM). Both of these methods

are generally applicable numerical methods of solving partial differential equations (for details on the wider scope of these methods see e.g. Brebbia and colleagues (2012) and Szabo and Babuška (1991), respectively). To apply the BEM method, the head is modelled as a piece-wise homogeneous volume conductor with K boundary surfaces separating regions of different conductivities (Fig. 10a & b). In the finite element method, the head is instead divided into a larger number of volumetric mesh elements where each element can have a unique conductivity (Fig. 10c). If the conductivity of live tissue is not known with high spatial precision, the main advantage of FEM does not apply. Thus BEM is the more popular method used in experimental MEG. While FEM is widely used in high-detail simulation studies it is considered out of scope for the purposes of this thesis and will not be covered in further detail.

To obtain the magnetic field in the piece-wise homogeneous model used in BEM, one applies the *Geselowitz formula* (Geselowitz, 1970):

$$\mathbf{B}(\mathbf{r}) = \mathbf{B}_0(\mathbf{r}) + \frac{\mu_0}{4\pi}\sum_{k=1}^{K}(\sigma_k^+ - \sigma_k^-)\int_{S_k}\phi(\mathbf{r}')\frac{(\mathbf{r}-\mathbf{r}')}{||\mathbf{r}-\mathbf{r}'||^3}\times d\mathbf{S}_k, \tag{8}$$

where σ_k^+ and σ_k^- correspond to the conductivities in the regions on the outer and inner side of the kth boundary, S_k is the surface of the kth boundary, the integration element dS_k is normal to that surface and the first term

$$\mathbf{B}_0(\mathbf{r}) = \frac{\mu_0}{4\pi}\int_{V'}\frac{\mathbf{J}_p(\mathbf{r}')\times(\mathbf{r}-\mathbf{r}')}{||\mathbf{r}-\mathbf{r}'||^3}dV' \tag{9}$$

is the contribution of the primary current $\mathbf{J}_p$ and the second term in Eq. 8 is due to the volume current $\mathbf{J}_v$. Eq. 8 holds for all location $\mathbf{r}$ not on the surfaces S_k, and from it one can see that the absolute conductivities of the different regions does not matter, only the difference across boundaries. Even more importantly, the potential ϕ only has to be calculated at the boundaries, thus decreasing the computational load considerably compared to FEM.

In order to calculate the effects of the volume conductor on $\mathbf{B}$, one has to compute the potential ϕ on the boundaries. For a location on a smooth boundary surface S_i, ϕ is formulated as (Ferguson & Stroink, 1997)

$$\phi(\mathbf{r}) = \frac{2\sigma_s}{\sigma_i^- + \sigma_i^+}\phi_0(\mathbf{r}) - \frac{1}{2\pi}\sum_{k=1}^{K}\frac{\sigma_k^- - \sigma_k^+}{\sigma_i^- + \sigma_i^+}\int_{S_k}\phi(\mathbf{r}')\frac{(\mathbf{r}-\mathbf{r}')}{||\mathbf{r}-\mathbf{r}'||^3}d\mathbf{S}_k, \qquad \mathbf{r}\in S_i \tag{10}$$

where ϕ_0 is the potential due to the primary current distribution if the conducting medium for the source is infinite in extent and has the conductivity σ_s. This conductivity value is usually only used to get the correct units for ϕ, and is thus set to 1. For primary current sources inside the volume conductor, ϕ_0 is

$$\phi_0(\mathbf{r}) = \frac{1}{4\pi\sigma_s}\int_{V'}\frac{\mathbf{J}_p(\mathbf{r}')\cdot(\mathbf{r}-\mathbf{r}')}{||\mathbf{r}-\mathbf{r}'||^3}dV'. \tag{11}$$

Thus, to calculate the magnetic field $\mathbf{B}(\mathbf{r})$ outside a volume conductor fulfilling the previously mentioned criteria, one applies Eqs. 11, 10, 9 and finally Eq. 8.

When modelling the head using BEM, one typically uses only a single boundary corresponding to the surface of the brain or three boundaries dividing the head into brain, skull and scalp. Using such a *multi-compartment model* provides more accurate results without any significant disadvantages (Stenroos et al., 2014). The geometries of these boundaries are determined through the segmentation of MR images. If MR images are not available, one can use a simpler spherical head model.

Pragmatically speaking, most heads fit reasonably well with a sphere. The use of a spherical model demonstrates several other attractive features (Sarvas, 1987). First and foremost, radially-oriented current sources are totally invisible outside the sphere, meaning that they are not seen in MEG. In reality, this is not strictly true due to the deviation of a real head from a sphere, but rather holds as a rule of thumb: while the sensitivity is not strictly zero, MEG has poor sensitivity to (pseudo-)radially oriented sources.

The conductivity values used for the different compartments come from the findings of several studies ranging from in-vitro to carcass examinations of tissue conductivity (e.g. Akhtari et al., 2002; Dannhauer et al., 2011; Lai et al., 2005; Zhang et al., 2006; Oostendorp et al., 2000). The conductivity of the skull is especially hard to pinpoint as the skull consists of several layers, which can be difficult to segment accurately from MR images. Fortunately the conductivity of the skull does not affect MEG to the same degree as in EEG (Stenroos & Hauk, 2013).

In addition to the skull, the layer of corticospinal fluid between the skull plays a significant role in modelling of cortical sources as it functions as a high-conductivity layer which allows for the volume current loops to close without going through the comparatively high-resistance skull. This effect is especially palpable in EEG, although it is not wholly insignificant in MEG (Stenroos & Nummenmaa, 2016). Thus, including the CSF as an additional, fourth BEM compartment might be advantageous if the CSF compartment can be properly identified in the MR images.

2.1.4 Inverse modeling

The previous section described how to derive the measured magnetic field knowing the neural sources, the so-called forward problem. The more common scenario of determining the neural sources when knowing the measured magnetic field is called the *inverse problem*. The inverse problem in MEG (and EEG), however, does not have a unique solution; there is an infinite number of combinations of sources that can give rise to any measured extracranial magnetic field. For example, in a spherical model any amount of radial currents can be present without affecting the extracranial magnetic field. In EEG, closed current loops within the head are similarly invisible. Thus, one must add constraints to the problem to produce a unique solution.

Dipole fitting

The simplest constrained solution to the inverse problem is to assume that the measured magnetic field is caused by a single current dipole, representing a small, focal activation of cortical tissue. To find the *equivalent current dipole* (ECD) that best fits the measured

data, least-squares minimisation of the error between the measured magnetic field and the magnetic field caused by the estimated dipolar activation is typically used (Baillet, 2010). As the measured magnetic field varies non-linearly with the position of the source, a non-linear search is used to adjust the position **r** and moment **Q** of the ECD. This single-dipole model can also be expanded to include several dipoles, although the correct estimation of several dipoles can be problematic, especially if they are temporally correlated (Salmelin, 2010).

Minimum-norm estimation

Another conceptually simple constraint is used in *minimum-norm estimation* (MNE), in which the either the $l1$- or $l2$-norm of the estimated source activity is minimised, meaning that the power ($l2$) or amplitude ($l1$) of the activation is minimised. Although this constraint has no immediate physiological basis, MNE has gained significant popularity due to its computational simplicity.

The source estimate $\tilde{\mathbf{j}}$, which satisfies the regularised minimum-$l2$-norm criterion is given by

$$\tilde{\mathbf{j}} = \mathbf{L}^T(\mathbf{L}\mathbf{L}^T + \lambda^2\mathbf{C})^{-1}\mathbf{b} \equiv \mathbf{G}\mathbf{b} \tag{12}$$

in which λ^2 is the regularisation parameter, **C** is the covariance matrix and **G** is the resulting inverse operator, which can be directly applied on the measured magnetic field **b**. As MNE is otherwise biased towards superficial areas, the regularisation parameter was used to rectify this as suggested by Lin and colleagues (2006):

$$\lambda^2 = \frac{tr(\tilde{\mathbf{L}}\tilde{\mathbf{L}}^T)}{N_c\overline{SNR}^2}, \tag{13}$$

where $\overline{SNR}$ is the average signal-to-noise ratio across all sources and $\tilde{\mathbf{L}}$ is the whitened lead field $\tilde{\mathbf{L}} = \mathbf{C}^{-1/2}\mathbf{L}$.

In practice, $l2$-MNE leads to large, diffuse estimates that typically overestimate the spatial spread of sources. In spite of these drawbacks MNE is a very robust and widely employed source localisation method.

Beamforming

Beamforming is another source estimation procedure, which was originally developed for directional transmission and reception of radio waves using spatial filtering. As applied for MEG (and EEG), spatial filters are designed as to pass signal related to brain activity (be it electrical or magnetic in nature) from a specified location while attenuating activity from all other locations. By designing filters for each location in the brain, one can achieve a spatial map of neural activity by depicting filter output as a function of passband location (Van Veen et al., 1997). Extensive reviews of the theory behind beamforming as applied to MEG and EEG can be found in the work by Hillebrand and Barnes (2005) as well as Huang and colleagues (2004).

Using a *linearly constrained minimum-variance* (LCMV) beamformer, an estimate of cortical source activity is made by weighted sum of magnetic field measurements

such that the estimated source amplitude $\tilde{j}$ at some point i in the source space is

$$\tilde{\mathbf{j}}_i = \mathbf{w}_i \mathbf{b} \tag{14}$$

where $\mathbf{w}_i$ is a vector of weighting parameters that are tuned specifically to the location i. $\mathbf{w}_i$ are formulated as to minimise the overall power in the signal estimated by the beamformer with the constraint that the power of a dipole source at the location i is conserved, thus creating a spatial filter with its pass-band at i. Mathematically, this can be written as

$$\min_{\mathbf{w}_i} E[\tilde{j}^2] \text{ subject to } \mathbf{w}_i \mathbf{L}_{\cdot,i} = 1, \tag{15}$$

where $\mathbf{L}_{\cdot,i}$ is the sensitivity for a source at location i, and for which the solution is given by (Van Veen et al., 1997; Hillebrand & Barnes, 2005)

$$\mathbf{w}_i^T = \frac{\mathbf{C}_d^{-1}\mathbf{L}_{\cdot,i}}{\mathbf{L}_{\cdot,i}^T \mathbf{C}_d^{-1}\mathbf{L}_{\cdot,i}} \tag{16}$$

where $\mathbf{C}_d$ is the data covariance. Using Eq. 14, the estimated power at i can be expressed as:

$$E[\tilde{j}_i^2] = P_i = E[(\mathbf{w}_i^T b)(\mathbf{w}_i^T b)^T] = \mathbf{w}_i^T \mathbf{C}_d \mathbf{w}_i. \tag{17}$$

Although one could directly use Eq. 17 to estimate the power of all sources across the source space, at deeper locations noise power will drown out any genuine sources due to the lower signal-to-noise ratio at these locations. As such the estimate will be biased towards deeper sources and needs to be normalised. Normalisation was implemented as described in the work by Sekihara and colleagues (2004) and Vrba and colleagues (2010), although several variations of this method exist (for a review, see Huang and colleagues (2004)):

$$Z_i^2 = \frac{\mathbf{L}_{\cdot,i}^T \mathbf{C}_d^{-1}\mathbf{L}_{\cdot,i}}{\mathbf{L}_{\cdot,i}^T \mathbf{C}_d^{-1}\Sigma\mathbf{C}_d^{-1}\mathbf{L}_{\cdot,i}} \tag{18}$$

where Σ is the sensor noise covariance (identical to the $\mathbf{C}$ used in Section 2.1.4) and Z_i^2 is the pseudo-Z statistic, or neural activity index, for location i.

2.1.5 Co-registration with MRI

For source estimation and visualisation of MEG data on a structural image of the brain, one needs to know the position of the sensors in relation to that image. The structural image in question is usually an MR image, which will need to be co-registered to the MRI data, i.e. the data from both modalities need to be transformed to a common coordinate system.

Co-registration is usually based on a set of *fiducial points* that can be identified in both data sets and thereafter aligned (George et al., 1989; Williamson & Kaufman, 1989). The fiducials most commonly used are the nasion and the preaurical points as defined in the 10-20 EEG electrode system (Jasper, 1958).

In current SQUID-based MEG systems, co-registration between structural MR images and MEG data is commonly performed using small *head position indicator* (HPI) coils that are positioned on the scalp of the subject either directly using an adhesive or on a head-band (Ahlfors & Ilmoniemi, 1989). Before the actual MEG measurement, a high-frequency current is fed into the HPI coils at different frequencies. The origin of the magnetic fields created by the coils can be localised using the MEG sensor array, just as it would be used to localise neural sources in the brain.

Unfortunately, the typical landmarks used in MRI (the nasion and preaurical points) are impractical as coil locations (Parkkonen, 2010); otherwise co-registration could be performed directly. Thus an intermediate coordinate system, the head coordinate system, is constructed. The HPI coil locations are added to this coordinate system using a 3D digitiser pen, along with the position of the fiducial points.

Additionally, the shape of the head can be registered by digitising a large number of points on the surface of the scalp. These head shape points can thereafter be matched to the head surface in the structural MRI. The surface-matching technique can be used in conjunction with the digitised landmark points (Whalen et al., 2008) or independently to co-register the head coordinate system to the MRI device coordinate system, while the HPI coil locations are used to co-register the head coordinate system to the MEG device coordinate system.

The HPI coils can also be energised continuously during MEG measurement to provide real-time head tracking (Nenonen et al., 2012), which is particularly useful for subjects with difficulty remaining still, e.g. children or epileptic patients. Other co-registration techniques have also been applied, such as using bite-bars (Adjamian et al., 2004) with HPI coils for a more easily reproducible co-registration when compared to HPI coils positioned on the scalp. The disadvantage of this technique is that all HPI coils are then positioned at the front of the head, which can magnify the effect of small errors.

An entirely different co-registration methodology was used by Troebinger and colleagues (2014), who created individualised 3D-printed head casts based on optical scans of the head shape and MR images, which fit into the helmet of the MEG system. Using these head casts together with MR-visible fiducial markers, accurate co-registration is possible and head motion during measurements is minimised. Additionally, the co-registration error between measurement sessions was also greatly diminished.

2.1.6 Comparison with other neuroimaging modalities

MEG shares many similarities with *electroencephalography* (EEG), in which instead of measuring the magnetic field outside the scalp, one measures the potential differences on the surface of the scalp caused by synchronised neural electric activity (Fig. 11). Although the signal measured by both of these neuroimaging modalities stems from the same sources, EEG is sensitive to both radially and tangentially oriented sources (Lopes da Silva, 2010), while MEG is primarily sensitive only to tangential sources.

In EEG, small electrodes coated in conductive electrode gel are placed on the scalp in an electrode array. This array, which commonly consists of 32–128 channels, is physically supported by either an electrode cap or a geodesic net of some sort. The

number of channels is typically lower than of a whole-head MEG array, as increasing the number of channels beyond 128 has diminishing returns (Song et al., 2015).

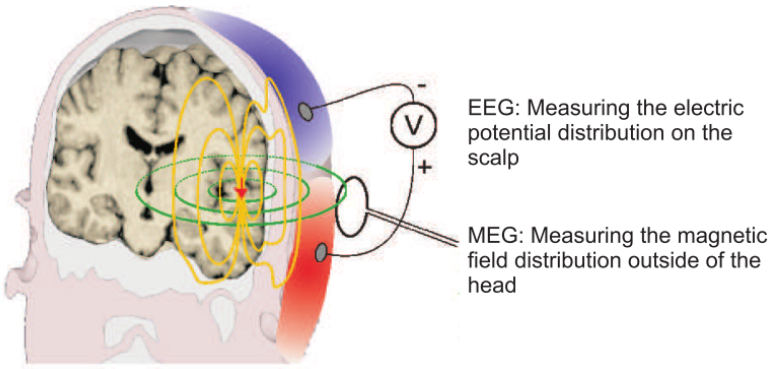

Figure 11: A neural source gives rise to scalp potentials (red and blue shadings) that can be measured using EEG and extracranial magnetic fields (green lines) that can be measuring using MEG. Reproduced from Parkkonen (2009).

EEG has comparable temporal resolution to MEG, i.e sampling rates can be several kHz, but its spatial resolution is slightly worse due to the relatively high-impedance skull 'smearing' the signal (Hämäläinen et al., 1993). Additionally, the CSF beneath the skull causes a shunting effect (Stenroos & Nummenmaa, 2016), partially closing the electrical loop of volume currents within the skull, thus weakening the EEG signal. MEG on the other hand is not as sensitive to these two phenomena.

In spite of the slightly worse spatial resolution of EEG, it has a number of advantages over MEG: First of all, the instrumentation is significantly less costly both to purchase and to maintain. EEG requires no cryogenics or even a MSR, although electromagnetic interference in the measurement room should still be minimised.

Many other forms of functional neuroimaging also exist. Perhaps the most widely used modality after EEG is functional MRI (fMRI), in which the changes in blood oxygenation due to neural activity, i.e. the *haemodynamic signal* is detected. fMRI has superior spatial resolution compared to both MEG and EEG and can also see deep neural activation imperceptible to the two former modalities. The temporal resolution of fMRI on the other hand is inherently limited to the scale of seconds (Kim et al., 1997) due to the sluggishness of the haemodynamic signal.

Many other functional neuroimaging modalities exist, but the comparison here is limited to the most common non-invasive methods as invasive methods represent a wholly different use-case scenario.

2.2 Optically-pumped magnetometers

Recent advances in atomic physics and diode lasers has enabled the development of *atomic magnetometers*, also known as *optically-pumped magnetometers* (OPMs) with high enough sensitivity to measure biomagnetic signals such as those of the brain (e.g. Xia et al., 2006; Shah & Wakai, 2013). The prime advantage of OPMs over the current SQUID sensors used in MEG is that they do not require any cryogenic cooling, and they can also be significantly miniaturised (Knappe et al., 2014). Specifically for MEG, the absence of a cryogenic dewar enables moving the sensors much closer the neural magnetic sources in the brain, thus boosting the signal-to-noise ratio (SNR) considerably.

The general principle in optical magnetometry, in very broad terms, is that light is used to measure the response of *atomic angular momentum* to the presence of magnetic fields (Kimball et al., 2013). Atomic magnetic moments μ emerge due to the magnetic moments associated with the intrinsic *spin* of electrons, atomic nuclei and orbital motion of electrons. When an external magnetic field B is applied, the torque

$$\boldsymbol{\tau} = \boldsymbol{\mu} \times \mathbf{B} \tag{19}$$

acts on the atoms. For small magnetic fields μ is independent of B, thus causing the angular momentum to *precess* around $\mathbf{B}$ at the Larmor frequency $\boldsymbol{\Omega}_L = \gamma \mathbf{B}$, where γ is the *gyromagnetic ratio* of the atom species in question. Applied light will interact with the atomic medium, exchanging angular momentum. Thus, the angular momentum of the light is affected by the angular momentum of the atomic medium, which in turn is driven by the precession caused by the external magnetic field. Using this relation, the precession of atomic angular momentum can be observed optically through the changes in intensity and polarisation of light propagating through the atomic medium.

In many OPMs, the resonant substance used as the core of the sensor is a vapour of alkali atoms (Rb, Cs or K) contained in a glass cell (Budker & Romalis, 2007). The medium needs to be polarised for a detectable signal to be acquired; the magnetometer signal scales linearly with the strength of atomic polarisation.

Atoms exhibit spontaneous polarisation due to thermal excitation. At room temperature, the thermal polarisation in the Earth's magnetic field ($\sim 50\ \mu$T) is $\sim 1 \times 10^{-7}$, which is too small to be used for magnetometry. In MRI, large magnetic fields in the order of several teslas are used to increase this polarisation, e.g. when increasing the magnetic field to 10 T the resulting thermal polarisation is 0.02. However, using a process called *optical pumping*, one can increase atomic polarisation to close to 1 (Seltzer, 2008). A light source, often a diode laser, is used as an *optical pump* (hence the name optically-pumped magnetometer) to polarise the alkali atoms. The polarisation is created by the photons from the resonant pump laser transferring their angular momentum to the alkali atoms, thereby creating polarisation in both ground and excited energy states (Kimball et al., 2013).

The emergence of ground-state polarisation is illustrated in an energy level diagram in Fig. 12. Consider a simplified scenario in which $\mathbf{B} = 0$ and a circularly polarised light beam illuminates the atomic medium. While the atoms in the ground state sub-level $+1/2$ cannot acquire any additional angular momentum, the ones in the ground state

sub-level $-1/2$ can absorb a photon from the pumping light source and jump to the excited state sub-level $+1/2$. These atoms very quickly spontaneously decay from their excited state, with the likelihood that they end up in the $-1/2$ sub-level being twice that of the $+1/2$ sub-level. However, if the pumping process continues and no other relaxation mechanism is in play all atoms will eventually be pumped to the $+1/2$ ground state sub-level. In the presence of a magnetic field, the atoms will coherently oscillate between the $-1/2$ and $+1/2$ sub-levels. This is the Larmor precession of the atoms about the magnetic field. (Happer, 1972; Kimball et al., 2013)

The above example illustrates the principle of optical pumping in a very simplified scenario: no relaxation mechanisms were taken into account and no magnetic field was present. For a detailed treatment of optical pumping and optical magnetometry, see e.g. Happer (1972) or Budker and Kimball (2013).

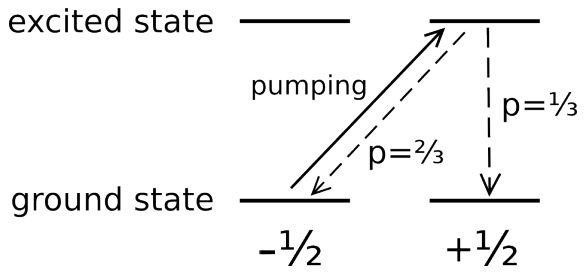

Figure 12: An example of an optical pumping scheme. Atoms from the $-1/2$ ground state sub-level are excited to the $+1/2$ energy sublevel of the excited state (solid arrow) whereafter they quickly decay to either of the ground state sub-levels (dashed arrows), eventually moving most or all atoms into the $+1/2$ ground state sub-level. Adapted from Seltzer (2008).

An archetypical all-out optical OPM (Fig. 13) uses two separate lasers: a circularly polarised pump laser and a linearly polarised probe laser. The pump laser is used to polarise the alkali metal vapour contained within a glass cell and the beam of the probe laser, after propagating through the alkali vapour, is detected by a photodiode. Using the photodiode signal, the change in polarisation or intensity due to precession of the polarised alkali vapour around the external magnetic field can be determined using a variety of methods (see e.g. Seltzer (2008)).

2.2.1 Sensitivity limits and noise

The fundamental limits of the sensitivity that can be achieved using OPMs are set by quantum fluctuations associated with the atoms in the alkali vapour and the photons of the probe and pump beams (Budker & Romalis, 2007; Seltzer, 2008). One such limit stems from the fact that if an atom is polarised in a particular direction, the measurement of angular momentum in an orthogonal direction will yield a random result ($\pm 1/2$ in the simplest case of angular momentum $F = 1/2$). The *spin-projection-noise-limited sensitivity* δB_{SNL} of an ensemble of N atoms and the *spin-relaxation rate*

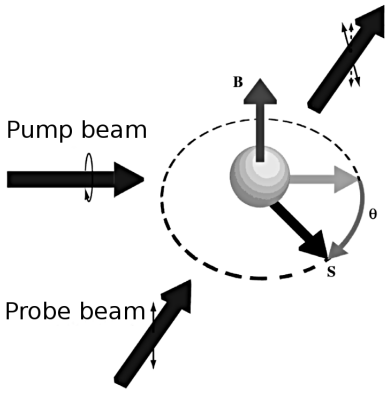

Figure 13: Typical arrangement of a (SERF) OPM, with a circularly polarised pump beam and a linearly polarised probe beam. Adapted from Savukov and Seltzer (2013).

Γ_{rel} for measurement times $\tau \gg \Gamma_{\mathrm{rel}}^{-1}$ is (Auzinsh et al., 2004)

$$\delta B_{\mathrm{SNL}} \approx \frac{1}{\gamma}\sqrt{\frac{\Gamma_{\mathrm{rel}}}{N\tau}}, \tag{20}$$

when ignoring some details of the atomic system involved. To understand Eq. 20 one can consider a simple example: the measurement of a single atomic spin with a duration of $\Gamma_{\mathrm{rel}}^{-1}$ produces an uncertainty of 1 radian. As is seen from Eq. 20, to maximise the highest possible sensitivity one should have the longest possible relaxation time for the atomic polarisation, i.e. the smallest possible Γ_{rel}, as well as the largest possible N. Therefore OPMs typically measure long-lived ground-state spin polarisation, and a range of methods can be used to minimise Γ_{rel}. The most common of these techniques include the usage of antirelaxation coatings, typically paraffin, on the walls of the vapour cell containing the atomic medium (Bouchiat & Brossel, 1966; Balabas et al., 2010) as well as filling the vapour cell with a buffer gas (typically He and/or N) to slow the diffusion of atoms to the cell walls (Brossel et al., 1955; Kimball et al., 2013).

Another contribution to noise in OPM measurements arises from the quantum uncertainty of measurements of the properties of light, i.e. *photon shot noise*. Optical detection of atomic spin precession is usually performed either through measurement of light transmission or of the polarisation of light transmitted through the sample. For example, if the measured quantity is the rotation angle ϕ of the light polarisation, the photon shot noise $\delta\varphi_s$ is (Budker & Romalis, 2007)

$$\delta\varphi_s = \frac{1}{2\sqrt{\Phi\tau}}, \tag{21}$$

where Φ is the probed photon flux (in photons per second) detected after propagating through the sample and $\delta\varphi_s$ is measured in rad/$\sqrt{\mathrm{Hz}}$.

Photon shot noise (Eq. 21) and spin projection noise (Eq. 20) contribute differing proportions of the overall measurement noise, although under optimal operating conditions photon shot noise does not exceed spin-projection noise (Auzinsh et al., 2004; Ledbetter et al., 2008). Another source of noise that can be a significant concern is

the AC Stark shift caused by the optical electric field of the circularly polarised pump laser (Happer & Mathur, 1967; Fleischhauer et al., 2000). Other sources of noise include environmental noise, technical noise relating to instrumentation and amplification, and finally thermal noise from nearby conductive materials (most commonly from materials used for magnetic shielding). In fact, many OPMs are not limited in sensitivity by any fundamental factors but rather by noise of technical nature (e.g. Kominis et al., 2003; Wyllie et al., 2012a)).

One way of improving OPM sensitivity is to increase the vapour density of the atomic medium. This typically requires an increase of the temperature of the cell, and as paraffin coatings do not work at higher temperatures than $\sim 80°C$ high-density cells typically use a buffer gas to mitigate the effect of alkali-atom–wall collisions on the relaxation rate (Budker & Romalis, 2007). As the density is increased, at some point the relaxation rate becomes dominated by collisions between alkali atoms within the cell and the quotient $\frac{\Gamma_{rel}}{N}$ approaches a constant so that spin-projection-noise-limited sensitivity no longer increases with density. As a result, a fundamental obstacle for improved sensitivity is reached for a given vapour cell volume.

2.2.2 Spin-exchange relaxation-free magnetometers

Collisions between alkali-metal atoms in a high-density OPM are typically dominated by *spin-exchange* (SE) collisions (Fig. 14) in which the electron spins of the individual colliding atoms rotate even though their combined spin is preserved. Although this type of collisions preserves total spin, they cause a loss of spin coherence. All alkali atoms have non-zero nuclear spin, and their ground states are split into a two-level hyperfine structure. The direction of magnetic precession for spins of the two hyperfine states is opposite, and thus SE collisions which randomly transfer atoms between the two hyperfine states results in macroscopic spin relaxation (i.e. loss of spin coherence) as the angles of angular momenta of atoms become random with respect to each other, thus cancelling out. (Budker & Romalis, 2007)

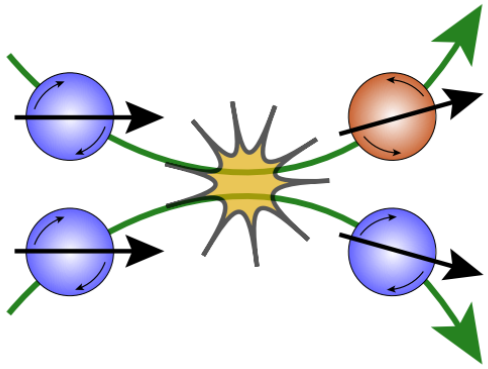

Figure 14: Total angular momentum is conserved during spin-exchange collisions, but one or both of the atoms may switch between hyperfine levels, leading to spin relaxation. The two hyperfine levels are represented here by the colours red and blue. Reproduced from Seltzer (2008).

It is possible to suppress the effects of SE relaxation by increasing the rate of SE collisions to such a degree that it exceeds the Larmor precession frequency (Happer & Tang, 1973; Happer & Tam, 1977). In this so-called spin-exchange relaxation-free (SERF) regime, one cannot speak of precessing atoms with a single hyperfine state, but rather an average precession in both of the two hyperfine states in the same direction as that of

a free atom in the upper hyperfine level. This is because atoms, on average, spend more time in the upper hyperfine level. Thus, in a weak magnetic field, the average angular momentum of the alkali vapour precesses without spin-exchange relaxation albeit at a slower rate than that of a free atom (Budker & Romalis, 2007).

One can only achieve operation in the SERF regime in very low magnetic fields, less than ~10 nT. In the SERF regime, vapour density can be several orders of magnitude higher than in conventional OPMs due to the absence of SE collisions. The relaxation rate is ultimately limited by spin-destruction (SD) collisions between alkali atoms, which do not conserve the total spin. (Budker & Romalis, 2007)

Sensor design

There has been considerable drive to miniaturise OPMs, aiming both to create sensors of smaller size and lower costs (Savukov & Seltzer, 2013). This type of sensor would be perfect for applications such as on-scalp MEG (see Fig. 15), since the sensors would need to be small to enable construction of a high-density sensor array. Diminished costs would also significantly lower the barrier of entry, as a large number of sensors are needed. This decrease in size and costs can be achieved through so-called "chip-scale" manufacturing, in which sensors would be fabricated in a similar manner to integrated semiconductor components.

Depending on the application, (chip-scale) optical magnetometers can either be constructed as self-contained, fully integrated units or as sensor heads connected using fibre optics to a central control unit. The centralised design is particularly suited for large sensor arrays, as it allows the use of a single pump (and probe) laser for all sensor heads, diminishing costs. (Savukov & Seltzer, 2013)

Figure 15: Four-channel array of microfabricated OPMs mounted on thermally insulating head cap. Reproduced from Knappe and colleagues (2014).

For the sensors themselves there exists a myriad of different designs. The design presented in Fig. 13 uses two lasers to achieve the highest possible sensitivity, although high sensitivity levels can also be achieved using only a single laser, which then functions both as a pumping and probing unit (Shah & Romalis, 2009).

To maintain the elevated temperature needed to function, especially at higher vapour densities, the alkali vapour needs to be heated. Several heating schemes have been devised: Some designs use electrical heating through resistive elements placed around the glass cell. When using electrical heating the effect of the heating current on the magnetic field measurements must be minimised. For example, the heating current can be driven at a frequency much higher than the bandwidth of the magnetometer. Alternatively, the heating currents can be turned off temporarily during measurements, thus limiting the continuous measurement time. Lastly, the heater elements can be pat-

terned in such a way that the interfering magnetic field is mostly cancelled out. (Savukov & Seltzer, 2013) Unfortunately none of these methods can be entirely noise-free, as any conductive material near the sensor will emit noise due to the thermal motion of electrons. Another option is to use optical heating, which allows for sensor heads that have only fibre-optical connections in a centralised design and is fully noise-free (Preusser et al., 2008). Additionally, thermal insulation around the vapour cell to minimise heat losses and in the case of MEG, allow close contact to the subject, is needed.

As SERF magnetometers can only function at low magnetic fields, even more care than in SQUID-based MEG needs to be taken to shield from interference and constant ambient magnetic fields. First of all, to achieve acceptable SNR levels, measurements will need to take place within a high-quality MSR. Mid-level commercial MSRs are not adequate for SERF operation, and will need additional active shielding. While SERF operation using only active shielding has been demonstrated (Seltzer & Romalis, 2004), the sensitivity levels achieved were unacceptable for MEG application. Due to the compactness of OPMs in comparison to the bulky dewar of SQUID-base MEG systems, it would also be possible to do measurements within a compact, human-sized magnetic shield. Such a compact MSR would cost significantly less than current, full-sized, MSRs (Xia et al., 2006).

SERFs have been operated within commercial MSRs using active shielding implemented both as a single tri-axial coil array (Johnson & Schwindt, 2010) and as smaller coil arrays integrated into each sensor (Wyllie et al., 2012b; Johnson et al., 2013). Both of these approaches have advantages and disadvantages. When deployed in a high-density sensor array as in MEG, the shielding fields of adjacent sensors may interfere with each other. On the other hand, a global shielding coil array may not be able to fully null the ambient magnetic field at every sensor, and even more importantly, if separate pump lasers for each sensor are used it cannot null the field caused by the AC Stark shift due to the optical pumping (Wyllie et al., 2012b).

Thus, a practical solution might be to use a large coil array to minimise the ambient field, and then use sensor-level coils to null the residual field and provide field modulation if required by the sensor design. (Iivanainen, 2016)

2.2.3 Comparison to SQUIDs

SERF and SQUID magnetometers are the most sensitive magnetometers for low-frequency signals (such as MEG) that have been developed. SQUID technology is very mature, and SQUIDs have been used in a variety of applications for decades, e.g. geophysical measurements (Schmidt et al., 2004), astronomy (Battistelli et al., 2008) and particle physics (Asztalos et al., 2010). SERF magnetometers, on the other hand, are still only at the early stages of their development. Judging by theoretical sensitivity, SERFs should be able to surpass SQUIDs and replace them in many applications. However, the comparison is not that simple.

First of all, the primary advantage of SERF magnetometers over SQUIDs is the fact that they do not need cryogenics to operate. Liquid helium is expensive and can be in short supply. The infrastructure and equipment needed for cryogenic operation can also be cumbersome and restrictive, e.g. for portable applications. Specifically for MEG,

noncryogenic operation allows for placing the sensors in much closer proximity to the head, thus boosting SNR and spatial resolution.

The use of cryogenics does offer some advantages as well, namely that it enables the use of superconducting flux transformers (SFTs). Using SFTs one can easily create gradiometers, thus removing uniform fields and noise from far-field sources. Synthetic gradiometers can also be created using several SERF magnetometers or by using multichannel detection (Savukov & Seltzer, 2013), although the benefits of doing so are not as substantial as with SQUIDs. One could also use SFTs in conjunction with SERF magnetometers, although as the prime advantage of SERF magnetometers is then lost. Additionally, the combination of cryogenic and high-temperature equipment can be problematic.

SERF magnetometers measure the absolute magnetic field, and cannot function in large ambient fields. SQUIDs on the other hand only measure relative field changes. Thus the dynamic range of SERF magnetometers is very limited compared to SQUIDs, which can operate even in the presence of large magnetic fields and gradients (Savukov & Seltzer, 2013). Negative feedback-based SERF systems that alleviate the problem of ambient magnetic fields have been demonstrated in principle, but have yet to match the sensitivity of open-loop systems. (Seltzer & Romalis, 2004; Knappe et al., 2014)

Another clear difference between SERF and SQUID magnetometers is their bandwidths. SERF magnetometers are inherently sensitive only in a narrow, low-frequency band, with a frequency response similar to that of a first-order low-pass filter (Knappe et al., 2014). The small bandwidth grants immunity to high-frequency noise, while SQUIDs require meticulous grounding and decoupling to avoid major issues (Savukov & Seltzer, 2013).

Finally, the use of SERF magnetometers may allow for interleaved transcranial magnetic stimulation (or any other pulse-based stimulation modality) and MEG measurement. This is because, SERF magnetometers can (at least in theory) quickly recover from the presence of strong, transient, magnetic pulses while SQUID sensors exhibit flux trapping or even breakdown of the junctions with very large magnetic fields.

2.3 Co-registration in on-scalp MEG

In this section, several methods to achieve accurate co-registration are examined both from the perspective of performance and practicality.

As described in Section 2.1.5, for source estimation to be possible, one must know the position and orientation of all sensors in relation to the head. In current SQUID-based MEG systems, the sensors are rigidly mounted, so that their positions in relation to each other and their orientations are known. In an on-scalp MEG system in which the positions of sensors are freely adjustable as to conform to the head size and shape of the subject, co-registration becomes more challenging due to the additional degrees of freedom involved: Instead of registering a single known set of sensors to the head one needs to independently register all sensors. To simplify the co-registration process, one may assume that all sensors are oriented normally to the scalp surface. To what degree this simplification would cause errors in source estimates remains to be seen. Co-registration error in current SQUID-based MEG systems is systematic in nature due to the rigid sensor array. In the type of on-scalp MEG system discussed in this work, sensor-wise location errors become apparent since they are individually localised and registered. Systematic errors on the other hand become more unlikely. Additionally, as the sensors in an on-scalp MEG system are in direct contact and move with the head of the subject, the need for continuous head tracking as in current SQUID-based MEG systems in which the head moves in relation to the entire sensor array (see Section 2.1.5) becomes less apparent.

2.3.1 Possible methods

Localisation of magnetometers in an on-scalp MEG systems is similar to the same procedure in EEG. The sensors are (to a degree) freely moveable in relation to each other, and conform to the shape of the subjects' scalp. The accuracy requirements for EEG co-registration may not be as high, as the poor (in relation to on-scalp MEG) spatial resolution masks the effect of co-registration errors (Michel et al., 2004). While the co-registration accuracy required for useful EEG source estimation is agreed to be roughly < 5 mm (Wang & Gotman, 2001; Koessler et al., 2007; Qian & Sheng, 2011), the required co-registration accuracy for on-scalp MEG systems is still unexplored.

Additionally, unlike in MEG, the orientation of EEG electrodes does not affect their sensitivity as long as the electrical contact is not unchanged. The physical characteristics of EEG electrodes differ significantly to those of SERF magnetometers, and the number of channels tends to be smaller in EEG measurements (most commonly 32 or 64). SQUID-based MEG systems on the other hand differ in that the sensors are rigidly mounted. Regardless, co-registration methodology as applied in current EEG and conventional MEG systems is bound to form the basis of co-registration methods used for on-scalp MEG.

Manual methods

In earlier EEG work, manual methods such as measuring the distances between all sensors using (digital) calipers (De Munck et al., 1991) or measuring the distances be-

tween a subset of sensors and thereafter interpolating the positions of the remaining sensors (Le et al., 1998). Such methods can be very time-consuming and error-prone. Interpolating the positions of sensors speeds up the process considerably but assumes that the sensors are arranged accurately in a known configuration. While manual methods do not require any specialised equipment they are inexpensive to implement, but alternative approaches may be preferable. Additionally, measuring the 3D orientation of all sensors using manual methods would be even more challenging and error-prone.

Electromagnetic digitisers

In current EEG systems, the electrode positions are commonly digitised using 3D digitisation tools (e.g. Brinkmann et al., 1998; Khosla et al., 1999; Le et al., 1998; Koessler et al., 2007). The same methodology is used in SQUID-based MEG (as described in Section 2.1.5) to digitise the location of HPI coils.

One common digitising tool is the Polhemus Fastrak (Polhemus Inc, Colchester, VT, USA, `http://polhemus.com/`), which works using a transmitter generating a near-field, low frequency (~8 kHz) alternating magnetic field through a single assembly consisting of three concentric, orthogonal coils. Two receivers are positioned within a digitiser stylus, which is moved to the points to be digitised. The receivers detect the magnetic field from the transmitter, whereafter both its position in relation to the transmitter and its orientation is computed from the magnitude and direction of the magnetic field detected by the receivers.

The Polhemus system can be quite precise, with the current Fastrak model having a specified location resolution of 0.00508 mm/mm of range (meaning a resolution of 1.524 mm at a operational distance of 30 cm from the transmitter) and an angular resolution of 0.15°. More importantly, the static root-mean-square (RMS) location error is specified as 0.762 mm for each axis. The maximum operational range is 120–160 cm. (Polhemus Incorporated, 2012)

When applied for EEG co-registration, digitisation errors of approximately 1–7 mm have been reported for the Polhemus Fastrak and earlier Polhemus models (see Table 1).

If a Polhemus-based co-registration system were to be implemented as currently applied in EEG, i.e. every magnetometer as well as the fiducial points were digitised, no other complications such as an intermediate coordinate system would be needed. To also determine the orientation of all sensors in relation to the head, at least two discrete points on each sensor would need to be digitised. The difficulty with such a system is the large amount of preparation needed for co-registration of the sensors, especially since one has to avoid shifting the sensors while digitising them. Considering that the time needed to digitise 64-channel EEG system is approximately 10 minutes (Koessler et al., 2007) the time needed to digitise all the MEG channels would be substantial.

Due to the nature of the Polhemus digitisation system, digitisation is performed outside the MSR prior to measurements. Depending on the physical properties of the on-scalp sensor array such as weight and size, there might be some risk of sensors shifting when moving the subject or during the experiment. Care also has to be taken to minimise electromagnetic noise and remove nearby large metallic objects, which can distort and reflect the Polhemus signal.

Ultrasonic digitisers

Ultrasonic 3D digitisers similar in practice to the electromagnetic ones described in the previous section have also been developed (e.g Huppertz et al., 1998). Ultrasonic digitisers work by measuring the time-lag for a sonic impulse to travel from a sound generator to several microphones. Using this travel time, the position of the sound generator can be triangulated. One example of such a device is the zebris ELPOS (zebris Medical GmbH, Isny im Allgäu, Germany, `http://www.zebris.de`), which has a specified position measurement accuracy of ±0.8 mm and a position resolution of approximately 0.1 mm (zebris Medical GmbH, 2005).

Ultrasonic digitisers have not gained much popularity, possibly due to their sensitivity to environmental factors such as humidity and temperature, as these factors affect the speed of sound through air.

Optical surface mapping

During the previous decades, several optical 3D surface mapping methodologies have been developed for use in industrial inspection, digitisation of physical models, interactive visualisation, and also for human body scanning in the field of medicine. These scanners can vary greatly in precision, cost and portability depending on the intended use and technology employed. Some of these methodologies are described below.

Photogrammetry Photogrammetry is a general-use optical 3D digitisation method, which has also been applied for EEG co-registration (Bauer et al., 2000; Russell et al., 2005; Koessler et al., 2007). Photogrammetry is used to determine the position of objects in three-dimensional space using photographic image data captured from a multitude of angles (Fig. 16). In practice, photographs are captured from several angles around the head either using a single rotating camera (Baysal & Şengül, 2010), an array of several cameras (Russell et al., 2005) or even a single camera coupled with a mirror array (Qian & Sheng, 2011). The primary advantage of photogrammetric methods is that each sensor does not need to be individually digitised, avoiding the need for accurate mechanical positioning of a digitiser stylus, which must be repeated for all channels. In addition, photogrammetry can be very quick. Instead of requiring several tens of minutes, the subject might only need to be stationary for as little as a second.

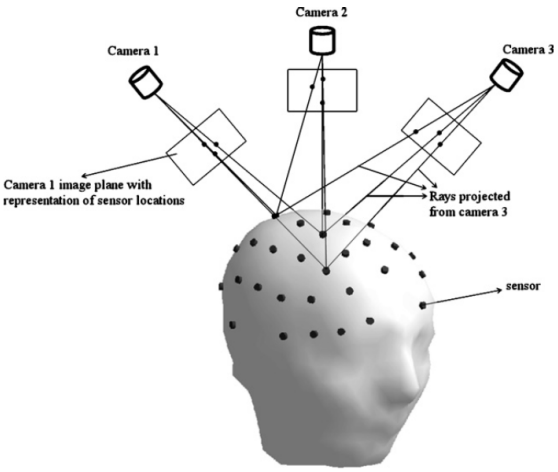

Figure 16: Operational principle of a photogrammetry system. Reproduced from Koessler and colleagues (2007).

Using photogrammetry one cannot usually digitise the entire surface of the head,

but rather only a smaller set of points of interest, i.e. sensors and fiducials. The largest challenge with photogrammetry is how to identify each sensor correctly in all images from different angles. As manually marking each sensor in all images would be far too laborous and error-prone, several automated approaches to this problem have been applied: a simple solution is to colour-code all electrodes (or other points of interest) (Baysal & Şengül, 2010; Qian & Sheng, 2011). The colour-coding approach allows full automation, although its feasibility for systems with a large number of channels is still to be demonstrated. Another way to identify sensors in photogrammetric digitisers is to attach small light markers, e.g. LEDs, to each sensor and sequentially capture photographs with only a single known marker lit (Bauer et al., 2000; Lamm et al., 2001). It is also possible to identify sensors without any specific marker system by utilising *a priori* information about the sensor array configuration, as done by Russell and colleagues (2005) for a 128-channel EEG array.

Structured-light scanning Structured-light scanning (Srinivasan et al., 1984) refers to a variety of optical surface mapping techniques which are based on the projection of structured light (different light-dark or coloured patterns, e.g. a sinusoidally striped pattern) onto an object and capturing the resulting patterns on the surface of the object using one or several cameras. The captured images are analysed using a variety of techniques (for a review, see Sai Siva Gorthi (2010)) through which the 3D shape of the object can be determined. A popular variation of structured-light scanning is fringe projection, which utilises a binary pattern of light-dark stripes. Fringe analysis techniques differ to some extent, but all rely on the fact that a fringe pattern projected onto a curved object will exhibit phase differences compared to that projected on a flat surface (see Fig. 17 for an example). Fringe projection systems can be very precise, e.g. commercial devices with a resolution of up to 100 μm and point accuracy of 50–100 μm (Artec Group Inc.; 3D-Shape GmbH) are available. However, this high precision can only be achieved if the subject is perfectly still, meaning that for MEG or EEG co-registration cumbersome and unpleasant immobilisation equipment has to be used or one risks compromised accuracy due to movement. Some variations of fringe projection are more motion-robust than others, but these tend to have lower resolution (Ettl, 2015).

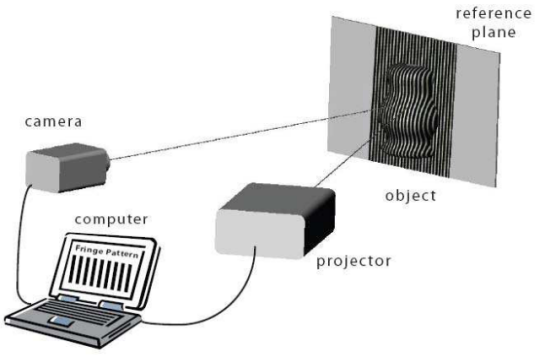

Figure 17: Basic fringe projection profilometry system. Reproduced from Sai Siva Gorthi (2010).

'Flying triangulation' (FlyTri, e.g. Ettl and colleagues (2012)) is a variation of fringe projection aimed at providing both motion robustness and resolution, something which existing fringe projection systems have not been able to deliver simultaneously. To achieve this, FlyTri uses a handheld device with a single-shot sensor to acquire sparse 3D data for each camera frame (Fig. 18). Sparse 3D data from individual camera frames are aligned without the use of any external tracking device. This is possible due to:

1) the assumption of smooth and reasonably small frame-to-frame movement and 2) alternation between horizontal and vertical stripe patterns for sequential camera frames, enabling accurate between-frames registration in spite of the sparse 3D data. In EEG co-registration, FlyTri has been shown to be more accurate (mean co-registration error 1.5 mm) as well as much faster than the conventional Polhemus system (Ettl et al., 2013; Dalal et al., 2014).

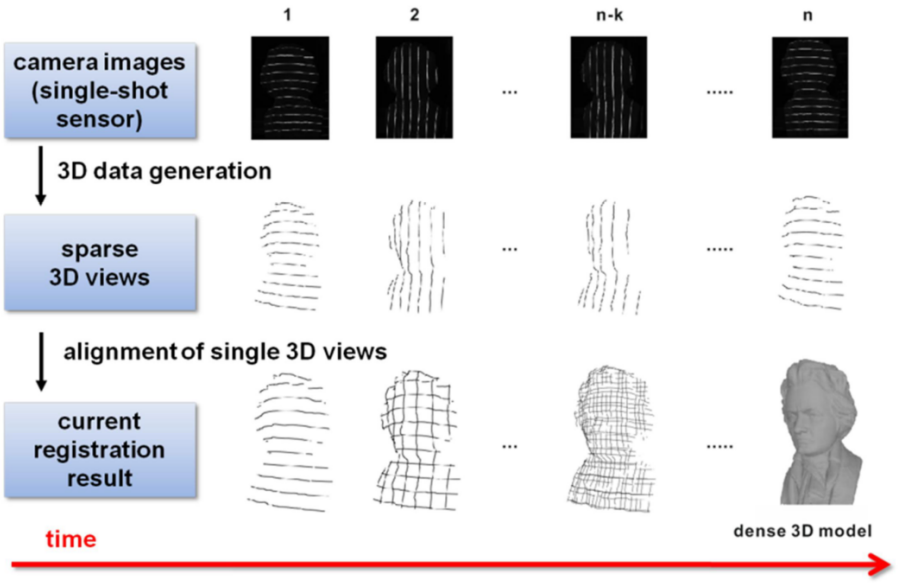

Figure 18: The measurement principle of 'Flying triangulation', a fringe projection variant consisting of sparse 3D data measured over time, which are then aligned and combined to a dense 3D model. Reproduced from Ettl and colleagues (2013).

Laser scanning Laser surface mapping utilises two cameras (or more) and one or several diode lasers which project cross-hairs on the surface to be digitised (Fig. 19). The distances between the cameras and the lasers are known and calibrated, and as such the position of the projected cross-hairs can be triangulated. To provide a reference point for a hand-held scanner, an array of reflective targets are affixed to the surface to be digitised. As long as the reflective targets are seen by the scanner it can be moved freely without the need for any tracking device. Subject motion during digitisation is not a problem either as long as the reflective targets do not shift. Hand-held laser scanners can be very accurate, e.g. the Handyscan 3D^{TM} by Creaform Inc. (Québec City, Canada) has a resolution of 0.05 mm and an accuracy of 0.03 mm (Creaform Inc., 2015).

Koessler and colleagues (2010, 2011) applied a laser scanner to co-register EEG with MRI, and showed that it provides equivalent accuracy and better repeatability than the Polhemus system when reflective targets were placed on each EEG electrode and on the fiducial points. Additionally, they digitised the upper part of the subjects' face and utilised this for more accurate co-registration with the structural MRI. They also showed that laser surface mapping can be much faster than the conventional Polhemus system: Digitising the fiducials and 64 sensor locations took less than a minute while the facial

surface mapping took ~2 minutes.

This same sensor localisation procedure could be applied to on-scalp MEG, although the same sensor *identification* problem as with photogrammetry still remains. To solve this problem, Koessler and colleagues (2010, 2011) applied *a priori* knowledge about the sensor array configuration to automatically identify all sensors on the scalp.

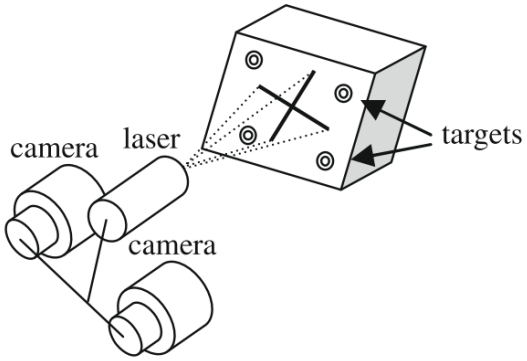

Figure 19: Handheld 3D laser scanner principle. At least four reflective target positions must be seen by the scanner at all times. Reproduced from Koessler and colleagues (2011).

Individualised head casts

Another option, which has already been explored for conventional MEG systems (Troebinger et al., 2014), is to use individualised, 3D-printed head casts for accurate co-registration. In the previous work, the interior shape of the head casts was determined by means of an optical scan of the subjects' head and face shape. This can be done e.g. by one of the techniques described above. Using optical scans one can include the space needed for the subjects' hair (held tight under a hair cap). The head cast was then co-registered to the head by digitising fiducial points and known points on the head cast using a Polhemus digitisation system.

In an on-scalp MEG system, the cast would have slots in which the sensors are inserted. The key factors in such a co-registration system are (a) that the proper shape of the head cast can be accurately determined and (b) that the proper shape can be accurately produced with small enough tolerances.

In case of inaccurate shape determination, a bad fit might lead to subject discomfort or movement during measurements. When using a head cast, movement during measurements is manifested as a systematic co-registration error, just as in current SQUID-based MEG systems.

Regarding the accuracy of production methods, using commercially available additive manufacturing (AM) equipment (i.e. "3D-printing"), one can achieve more than sufficient resolution of < 200 μm on all axes (Wong & Hernandez, 2012).

The primary drawback of using head casts for co-registration is the logistics involved. Head cast modelling will presumably involve manual adjustments as well as additional optical scanning equipment, and as the required AM equipment is both bulky and expensive, the casts need to be produced by a third party. Thus, experimental work using this co-registration workflow is significantly more cumbersome as subjects first need to be called to the laboratory for MR imaging and optical head scanning, the head cast needs to be modelled and ordered, and only when it arrives can the actual MEG measurements be performed.

On the other hand, the use of structurally robust head casts also solves another challenge of on-scalp MEG: how to support the sensors, which are considerably larger and

heavier than EEG electrodes, on the subjects' head without any sensor-wise movement during measurements.

Gradient-based methods using shielding coil array

If a global active shielding system within the MSR is used to keep the magnetometers within the SERF regime, the same coils can be used to create magnetic gradients. The measured magnetic field at each sensor can then be used to calculate the position of each sensor. This method was applied by Kim and colleagues (2014) in conjunction with a multichannel SERF OPM-based MEG system to calculate the effective position of each channel in two dimensions.

More extensive implementations of this technique using OPMs have yet to be demonstrated, although in theory, such a set-up allows for real-time sensor position tracking, as long as the magnetic gradients used for tracking do not interfere with actual MEG measurements. Here, the small bandwidth of SERF OPMs may be a hindrance, as high-frequency modulated fields cannot be used in the same way as for real-time head position tracking in SQUID-based MEG.

The methodology presented here cannot be used directly for co-registration as only the position of the sensors, not the head, can be determined. Either one has to place a number of sensors at known anatomical locations (i.e. the fiducials) or a complementary sensor localisation method has to be used. The primary utility of the gradient-based tracking would then be real-time tracking of head movement.

2.3.2 Summary and comparison of methods

A summary of all the possible sensor localisation methods presented here can be seen in Table 1. As is clearly seen in the table, many studies have compared new, unproven methods to the established and widely used Polhemus digitisation tools.

When comparing the procedure time as presented in Table 1, one should take into account the sensor array in question; if it is EEG, the number of channels is most relevant. Some of the studies utilising optical scanning methods also performed face shape digitisation for enhanced co-registration accuracy. While such additional digitisation is also possible using e.g. the Polhemus system, the additional time needed might pose a practical problem.

Table 1: Summary and comparison of examined sensor localisation methods as applied for EEG/MEG co-registration.

Study	Method	Sensor array	Subjects	Reported accuracy		Duration	Sensor identification
				Measurement	Co-registration		
De Munck et al. (1991)	Direct measurement (calipers)	-	-	< 2.5 mm[a]	-	-	-
Le et al. (1998)	Direct measurement (calipers)	64-channel EEG	11	-	-	> 1 h	-
Le et al. (1998)	Direct measurement and interpolation[b]	64-channel EEG	11	3.0 mm[c]	-	5.66 ± 0.67 min	-
Le et al. (1998)	RF digitiser (Polhemus[d])	64-channel EEG	11	3.6 mm[c]	-	7.95 ± 0.79 min	-
Towle et al. (1993)	RF digitiser (Polhemus[d])	20-channel EEG	4	1.4 mm	-	-	-
Brinkmann et al. (1998)	RF digitiser (Polhemus[d])	21-channel EEG	phantom	0.9 ± 0.67 mm[e]	-	-	-
Brinkmann et al. (1998)	RF digitiser (Polhemus[d])	21-channel EEG	5	-	3.09 ± 1.44 mm[e]	-	-
Russell et al. (2005)	RF digitiser (Polhemus Fastrak)	128-channel EEG	4	1.02 ± 0.04 mm	-	25-35 min	-
Whalen et al. (2008)	RF digitiser (Polhemus Fastrak)	32 MR-visible markers	6	0.8 mm	1.3 ± 0.1 - 4.4 ± 0.6 mm[f]	-	-
Baysal & Şengül (2010)	RF digitiser[d]	25 EEG markers	phantom	7.66 ± 3.83 mm[g]	-	15 min	-
Koessler et al. (2010)	RF digitiser (Polhemus Fastrak)	64-channel EEG	5	2.92 ± 1.06 mm	-	-	-
Ettl et al. (2013)	RF digitiser (Polhemus Fastrak)	68-channel EEG	phantom	3.39 mm	-	-	-
Dalal et al. (2014)	RF digitiser (Polhemus Fastrak)	68-channel EEG	phantom	6.8 mm	-	-	-
Hironaga et al. (2014)	RF digitiser (Polhemus Fastrak)	MEG, 6 HPI coils	11	-	1.01 ± 0.3 mm[f]	-	-
Huppertz et al. (1998)	Ultrasonic digitiser (zebris ELPOS)	64-channel EEG	20	-	3.39 ± 0.24 mm	10 min	-
Bauer et al. (2000)	Photogrammetry	-	-	0.18 ± 0.29 mm	2.29 mm	< 1 s	LED markers
Russell et al. (2005)	Photogrammetry	128-channel EEG	4	1.27 ± 0.08 mm	-	a few seconds	Algorithmic
Baysal & Şengül (2010)	Photogrammetry	25 EEG markers	phantom	0.41 ± 0.18 mm	-	4.5 min	Coloured markers
Qian & Sheng (2011)	Photogrammetry	25 EEG markers	phantom	0.59 ± 0.31 mm	-	3 min	Coloured markers
Ettl et al. (2013)	Structured-light scanning ('FlyTri')	68-channel EEG	phantom	0.89 mm	-	-	Manual
Dalal et al. (2014)	Structured-light scanning ('FlyTri')	68-channel EEG	phantom	1.5 mm	-	-	Manual
Koessler et al. (2010)	Laser scanning	64-channel EEG	5	1.21 ± 0.58 mm	-	3 min[h]	Algorithmic
Koessler et al. (2011)	Laser scanning	64-channel EEG	5	1.21 ± 0.58 mm	2.11 ± 0.46 mm	3 min[h]	Algorithmic
Hironaga et al. (2014)	Laser scanning	MEG, 6 HPI coils	11	-	0.615 ± 0.125 mm[f]	< 5 s	-
Troebinger et al. (2014)	Individual head casts + Polhemus Fastrak	MEG, whole head array	2	-	1-2 mm	-	-

[a] Standard deviation. Not tested, only assumed.
[b] Assumes known sensor array configuration.
[c] Golden standard was direct measurement.
[d] Exact model not disclosed.
[e] Estimated fiducial localisation error.
[f] Target registration error.
[g] Non-expert operator.
[h] Including face shape scanning, 53 s without.

3 Simulations

Simulations were performed to examine the effect of random error in the locations of OPMs in the sensor array as to determine the required sensor localisation accuracy needed for accurate source estimation in on-scalp MEG. To this end, a hypothetical 184-OPM sensor array with each sensor measuring the normal component of the magnetic field was constructed and several types of source estimation simulations were performed.

3.1 Anatomical models

T1-weighted magnetic resonance images were obtained from ten healthy adults (7 males, 3 females) using a 3T MRI scanner and an MP-RAGE pulse sequence. The Freesurfer software package (Dale et al., 1999; Fischl et al., 1999a; Fischl, 2012) was used for pre-processing the MRI images and segmentation of the cortical surface.

For each subject, a watershed algorithm (Ségonne et al., 2004) implemented in Freesurfer and MNE software (Gramfort et al., 2014) was used to segment the brain, skull and scalp surfaces. These surfaces were thereafter decimated to obtain three boundary element meshes (2 562 vertices per mesh). The neural current sources were assumed to lie on the cortical surface, and thus a source space consisting of a 5th-grade icosahedral mesh (10 242 vertices per hemisphere) was constructed upon the cortex. For the sake of visualisation and group-level statistics, individual brains were mapped to an average template brain using the spherical morphing procedure in Freesurfer (Fischl et al., 1999b).

3.2 Sensor models

Each optically-pumped magnetometer was modelled as a set of eight discrete integration points, set in space as to be uniformly distributed in the volume of a hypothetical cube-shaped sensor with a side-length of 5 mm (coordinates with the origin set in the centre of the bottom face of the cube: ± 1.25 mm, ± 1.25 mm, 1.25/3.75 mm). Equal weight (1/8) was given to each integration point, meaning that the output of each sensor was the average of the numerically determined magnetic field components at these points.

3.3 Construction of sensor arrays

The sensor arrays were constructed by adapting a set of 184 locations on a unit sphere, chosen as to resemble a typical MEG sensor helmet, onto the scalp surfaces of individual subjects. The spacing of the sensors, and thus the number of sensors in the array, was decided on the basis of a hypothetical sensor with outer dimensions of 20 x 20 mm^2 on the scalp plane. The distance of the sensors from the scalp was set to 1 mm. The sensors were oriented as to measure the normal component of the magnetic field with respect to the scalp.

From the original sensor array constructed for each subject, displaced sensor arrays with a sensor-wise random location error were constructed. Each sensor in a displaced

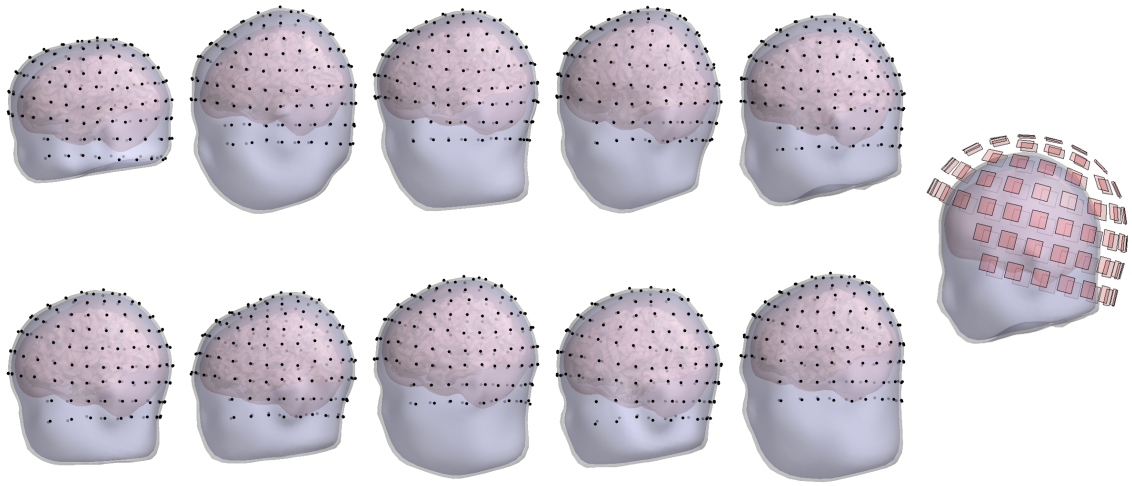

Figure 20: Scalp, skull and brain compartment BEM meshes of all subjects and points depicting OPM sensor array (left). One subject with 306-channel state-of-the-art SQUID-based MEG system included for comparison (right).

array was moved a random amount within a circle on a plane which was tangential to the scalp, according to a constant probability density function within that circle. The radius of the circle represented the uncertainty in the location of the sensors, and maximum uncertainties of 2.5, 5, 10 and 20 mm were examined. For each simulated level of uncertainty, 50 different displaced sensor arrays were constructed for each subject, resulting in q grand total of 500 displaced sensor arrays per level of uncertainty.

In addition to all the OPM-based sensor arrays, a 306-channel (102 magnetometers, 204 planar gradiometers) SQUID-based MEG sensor array based on actual MEG measurements were obtained for all subjects. These arrays were to be used as a comparison baseline.

3.4 Forward models

Measured magnetic fields **b** are related to the neural sources by Eq. 1, i.e.

$$\mathbf{b} = \mathbf{L}\mathbf{j},$$

where **L** is the lead field matrix. The lead field matrix describes the sensitivity — *or gain* — of each sensor to a unit dipole at each location of the source space. The matrix is organised as such that each column i represents the topography of source i (how the sensors sees that source), while each row j represents the sensitivity of sensor j to all sources.

Lead-field matrices were computed for each subject and sensor array using the linear Galerkin boundary element method (BEM) with an isolated source approach (ISA) as described by Stenroos and Sarvas (2012). The Galerkin BEM is computationally more costly, but superior in performance to the commonly used point collocation BEM. The use of ISA, which first treats the skull as a perfect insulator whereafter a

correction factor is added, alleviates numerical instabilities due to the large differences in conductivity across compartment boundaries. The conductivities of the brain, skull and scalp compartments were assumed to be $[1, \frac{1}{25}, 1] \cdot \frac{1}{3}$ S/m.

3.5 Metrics

Several measures were used to quantify the effect that sensor location error has both on the lead fields (i.e. the forward models) and the source estimates calculated using these lead fields (i.e. the inverse models).

3.5.1 Forward metrics

Relative error (RE) is a measure which is sensitive to both morphological and amplitude errors in the lead fields. The relative error for the source i is formulated as

$$\mathrm{RE}_i = \frac{||\mathbf{L}^{\mathrm{ref}}_{\cdot,i} - \mathbf{L}^{\mathrm{test}}_{\cdot,i}||}{||\mathbf{L}^{\mathrm{ref}}_{\cdot,i}||}, \tag{22}$$

where $\mathbf{L}^{\mathrm{ref}}_{\cdot,i}$ and $\mathbf{L}^{\mathrm{test}}_{\cdot,i}$ are the reference and test topographies of an unit source (ith columns of the lead-field matrices $\mathbf{L}^{\mathrm{ref}}$ and $\mathbf{L}^{\mathrm{test}}$, respectively) and $||\cdot||$ is the $l2$-norm.

To further investigate the morphological differences between lead fields, the correlation coefficient (CC) between the sensitivities to all individual sources was calculated. The correlation coefficient for source i as applied by Haueisen and colleagues (1997); Stenroos and Sarvas (2012) is expressed as

$$\mathrm{CC}_i = \frac{\mathbf{L}^{\mathrm{ref}}_{\cdot,i} - \overline{\mathbf{L}}^{\mathrm{ref}}_{\cdot,i}}{||\mathbf{L}^{\mathrm{ref}}_{\cdot,i} - \overline{\mathbf{L}}^{\mathrm{ref}}_{\cdot,i}||} \cdot \frac{\mathbf{L}^{\mathrm{test}}_{\cdot,i} - \overline{\mathbf{L}}^{\mathrm{test}}_{\cdot,i}}{||\mathbf{L}^{\mathrm{test}}_{\cdot,i} - \overline{\mathbf{L}}^{\mathrm{test}}_{\cdot,i}||}. \tag{23}$$

Furthermore, we can calculate the peak position error (PPE) of all sources, which describes the dislocation of the centre-of-mass of similar-topography sources. PPE is expressed as (Stenroos & Hauk, 2013)

$$\mathrm{PPE}_i = \left|\left|\mathbf{r}_{\mathrm{ref}} - \frac{\sum_i ||\mathrm{CC}_i||\mathbf{r}_i}{\sum_i ||\mathrm{CC}_i||}\right|\right|, \tag{24}$$

where the sum is taken across sources with considerable correlation (absolute value of $\mathrm{CC} \geq 0.9$), CC_i is the correlation coefficient between the reference source and the source i, $\mathbf{r}_i$ and $\mathbf{r}_{\mathrm{ref}}$ are the locations of the source i and the reference source, respectively. As applied here, $\mathbf{L}^{\mathrm{ref}}$ is the lead field matrix of the original sensor array, while $\mathbf{L}^{\mathrm{test}}$ is the lead field matrix of a displaced sensor array.

3.5.2 Inverse metrics

MNE

Minimum-$l2$-norm estimates, as defined in Eq. 12, were used as a basis for several source localisation metrics. For the regularisation (see Eq. 13), the mean SNR of all

sources was set to 3. No noise other than sensor noise was taken into account in the source estimation. Thus the covariance matrix **C** was a diagonal matrix with the diagonal elements being the noise variance of the sensors. The noise variance of the OPMs was set to 10 fT/$\sqrt{\text{Hz}}$, as this was deemed reasonable considering the reported noise levels of actual microfabricated sensors (Shah & Wakai, 2013; Alem et al., 2014).

The measures used to investigate the effect of sensor localisation error on the minimum-$l2$-norm source estimates are based on the concept of a resolution matrix as applied in earlier literature (Grave De Peralta Menendez et al., 1997; Hauk et al., 2011; Stenroos & Hauk, 2013):

$$\mathbf{K} = \mathbf{GL}, \tag{25}$$

where **G** is the MNE inverse operator (see Eq. 12). The columns of the resolution matrix **K** consist of the point spread functions (PSFs) of each source, which describe how the activation of each source is seen in the source estimate. The rows of the resolution matrix represent cross-talk functions, which describe how each source can contribute to activity seen in a single point in the source estimate. Here, a resolution matrix was computed for each displaced sensor array using the inverse operator of the original sensor array together with the lead field of each displaced sensor array, thus simulating the effect of error in sensor location.

By replacing the CCs in Eq. 24 with the PSFs of the resolution matrix, the localisation performance of the inverse estimators for each sensor array was assessed by computing the PPE of the source estimates:

$$\text{PPE}_i = \left|\left|\mathbf{r}_{\text{ref}} - \frac{\sum_i ||\text{PSF}_i||\mathbf{r}_i}{\sum_i ||\text{PSF}_i||}\right|\right|. \tag{26}$$

The PSFs were thresholded by only including the points at which $|\text{PSF}_i| \geq 0.5\text{PSF}_{\text{max}}$. As PPE only elucidates the topological aspects of the PSFs, the correlation between the PSFs of the resolution matrix computed for the original sensor array and of those with displaced sensor arrays was computed using an adapted version of Eq. 23:

$$\text{CC}_i = \frac{\text{PSF}^{\text{ref}}_{\cdot,i} - \overline{\text{PSF}}^{\text{ref}}_{\cdot,i}}{||\text{PSF}^{\text{ref}}_{\cdot,i} - \overline{\text{PSF}}^{\text{ref}}_{\cdot,i}||} \cdot \frac{\text{PSF}^{\text{test}}_{\cdot,i} - \overline{\text{PSF}}^{\text{test}}_{\cdot,i}}{||\text{PSF}^{\text{test}}_{\cdot,i} - \overline{\text{PSF}}^{\text{test}}_{\cdot,i}||}, \tag{27}$$

thus quantifying the morphological effect of the sensor position error.

Beamformer simulations

In addition to the minimum-norm estimates, LCMV beamformer estimates were performed using a similar methodology to that used by Brookes and colleagues (2008); Hillebrand and Barnes (2003, 2011).

Datasets were constructed in which sources were placed one at a time at vertices of a 3rd-degree icosahedral mesh (684 source points per hemisphere). Although a 5th-degree icosahedral mesh was otherwise used for the source space, here the sparser mesh was used to keep the problem computationally tractable.

For each dataset, a single source was given a 40-Hz sinusoidal activation profile with unit peak amplitude. To approximate a realistic experimental scenario, white Gaussian

noise was added to the simulated magnetic field. The noise variance for a given SNR level was determined using the definition of local SNR of Goldenholz and colleagues (2009):

$$\mathrm{SNR}_j = \frac{a^2}{N} \sum_i \frac{L_{j,i}^2}{\sigma_j^2}, \tag{28}$$

where a is the source amplitude, N is the number of sensors and σ_j^2 is the noise variance of sensor j. When the source is of unit amplitude and all sensors have identical noise variance, this equation simplifies to

$$\mathrm{SNR}_j = \sum_i \frac{L_{j,i}^2}{\sigma^2 N}. \tag{29}$$

Since we want to define our noise variance according to the *global* SNR, not the local one, we take the average over all sensors, leading to

$$\mathrm{SNR} = \sum_j \frac{\mathrm{SNR}_j}{N} = \sum_j \sum_i \frac{L_{j,i}^2}{\sigma^2 N^2} \tag{30}$$

from which we can easily solve for σ^2 according to the desired SNR. This procedure is equivalent to empirically setting $SNR = \frac{\sigma_{\mathbf{b}}^2}{\sigma^2}$, where $\sigma_{\mathbf{b}}^2$ is the variance of $\mathbf{b}$. As beamformers are commonly applied to unaveraged data the SNR was set to a relatively small value of 0.1. For each dataset, 1 s of activity sampled at 600 Hz (600 samples) was simulated. The estimated pseudo-Z^2 statistic (Eq. 18) was used as a single source localisation estimate over the entire simulated time window.

To examine the effect of sensor position error, the "measured" magnetic field $\mathbf{b} = \mathbf{Lj}$ was computed using the lead field of the original sensor array while the Z^2-statistic (Eq. 18) was computed using the lead field of a displaced sensor array.

The error due to the displacement of sensors, i.e. beamformer position error (BPE), was quantified in a straightforward manner by the distance between the location with the maximal Z^2-statistic and the location of the true source:

$$\mathrm{BPE}_i = ||\mathbf{r}(Z_{\max}^2) - \mathbf{r}_i||. \tag{31}$$

Dipole localisation

Additional source estimation simulations in the form of least-squares dipole fitting with free source orientation were carried out. As for the beamformer simulations, sources were placed on a 3rd-degree icosahedral mesh although a 5th-degree mesh was used for source localisation. Unlike in the MNE and beamformer simulations, the simulated dipole orientation was random and the lead fields used were not projected as comprise only sources that are normally oriented to the cortex but included the sensitivity in all axes. As with the earlier inverse models, localisation was cortically constrained to the points of the source space.

As with the LCMV beamformer simulations, to approximate a realistic experimental scenario, white Gaussian noise was added to the simulated magnetic field as to achieve several different levels of SNR.

To simulate the effect of sensor position error, the measured magnetic field was computed using the lead field of the original sensor array while the lead field of a displaced sensor array was used for the dipole fit procedure.

To quantify the impact of sensor array inaccuracies on the source localisation, dipole position error, i.e. the three-dimensional Euclidean distance between the fitted and actual dipoles was used. In a similar manner, the dipole orientation error was defined as the difference in orientation between the actual and fitted dipole. Finally, the goodness-of-fit (GOF) of the fitted dipoles, i.e. how well they explain the original data, was compared.

4 Results

If not otherwise mentioned all metrics were calculated individually for each subject and each sensor array for that subject. Metrics were thereafter morphed to the average brain where the data were averaged across subjects. The colour scales of the graphs in this section were chosen as to be maximally informative; in the case that a colour scale does not fully encompass the range of values that are present in the data one can use the histograms accompanying graphs to see the full range of the data. The level of sensor position error in each simulation is reported through both the maximum error and the RMS error. For some metrics in this section, sources may be split into deep and shallow categories (Fig. 21). The classification boundary for this division was defined such that sources deeper than 30 mm from the scalp were classed as deep while others were classed as shallow.

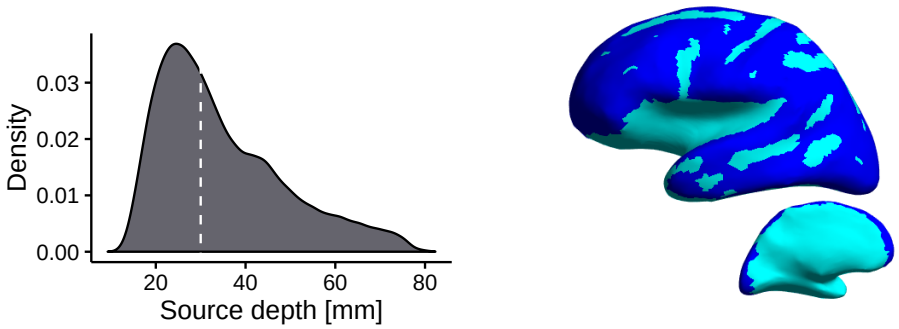

(a) (b)

Figure 21: (a) Source depth for all subjects, measured from the surface of the scalp. The white dotted line represents the 30-mm depth at which sources were split into shallow and deep. (b) Average of source depth for all subjects, thresholded to show which areas are classified as deep (light blue) and superficial (dark blue).

4.1 Forward metrics

The relative error (RE) for lead fields due to the random displacement of sensors can be seen in Fig. 22. This error is larger in superficial areas, which is to be expected as these areas are closer to the sensors that are being displaced. The mean RE when the maximum sensor-wise error is 2.5 mm is 5.43%, growing to 12.24% and 21.30% when the error is increased to 5 mm and 10 mm, respectively. When the maximum sensor-wise error is 20 mm the mean RE is 40.35%.

Similarly, the morphological change of the forward models due to sensor-wise error (Fig. 23) is mostly apparent in the areas of high sensitivity. The mean CC when the maximum sensor-wise error is 2.5 mm is 0.9984, falling to 0.9915 and 0.9753 when the error is increased to 5 mm and 10 mm, respectively. When the maximum sensor-wise error is 20 mm the mean CC is 0.9093.

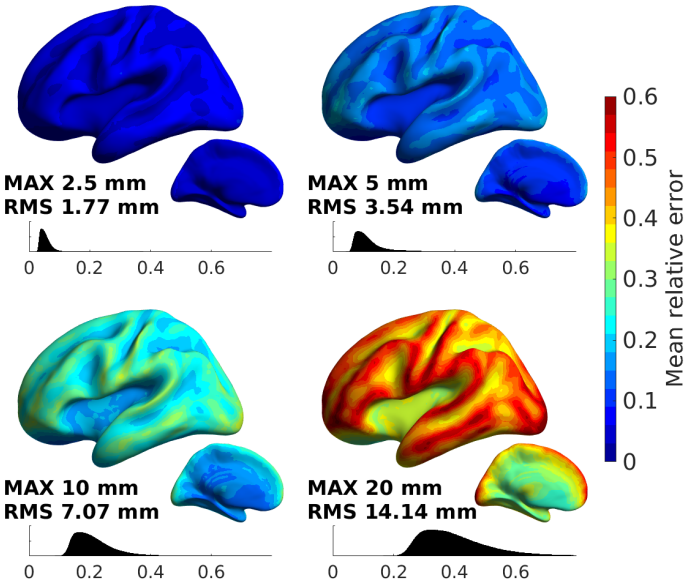

Figure 22: Average relative error of lead fields over all subjects. Although only the left hemisphere is shown, the histograms include data from both hemispheres.

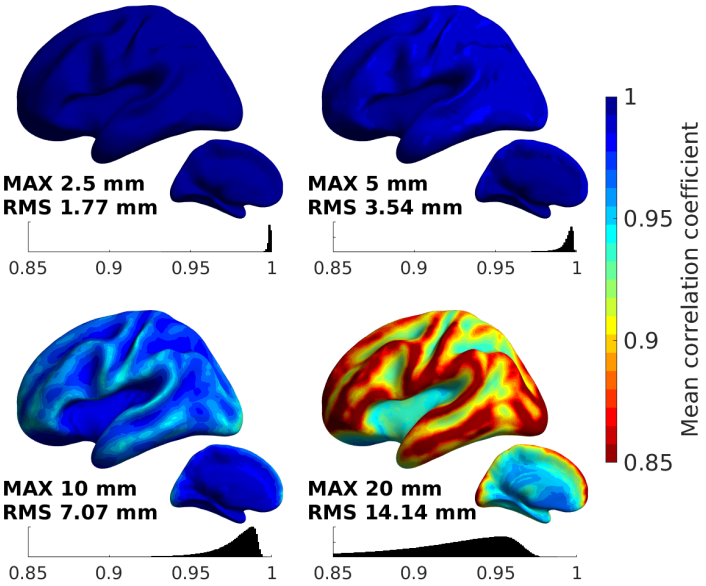

Figure 23: Average correlation coefficients of lead fields over all subjects. Although only the left hemisphere is shown, the histograms include data from both hemispheres.

4.2 Inverse metrics

4.2.1 MNE

Results for both the peak position error and correlation coefficient of PSFs can be seen in Table 2. As with the correlation coefficient for the forward models, the largest morphological errors in the MNE point spread functions (PSFs) are seen in superficial

Table 2: Peak position errors and correlations coefficients of point-spread functions computed from the MNE resolution matrix.

Maximum sensor position error (sensor array)	Shallow sources		Deep sources		All sources	
	PPE [mm]	CC	PPE [mm]	CC	PPE [mm]	CC
Reference (OPM)	5.0	-	19.2	-	12.6	-
2.5 mm (OPM)	5.2	0.9953	19.4	0.9980	12.8	0.9927
5 mm (OPM)	5.7	0.9656	19.9	0.9878	13.3	0.9775
10 mm (OPM)	6.8	0.8817	20.6	0.9518	14.2	0.9192
20 mm (OPM)	9.2	0.6145	22.1	0.8462	16.1	0.7386
Reference (Mag-SQUID)	5.2	-	18.5	-	12.3	-
Reference (All-SQUID)	5.1	-	19.3	-	12.7	-

areas (Fig. 24, Table 2).

The average PPE over all subjects (Fig. 25) is very large for deep sources, on the order of tens of millimeters, regardless of sensor position error. The PPEs for shallow sources are much smaller, but are also considerable in size when no sensor position error is present. As a comparison, the PPEs for Elekta's 306-channel (102 magnetometers, 204 planar gradiometers) SQUID-based MEG system were also calculated without any sensor position error, both using all 306 channels ("All-SQUID" in Table 2) and when only utilising the 102 magnetometers ("Mag-SQUID" in Table 2).

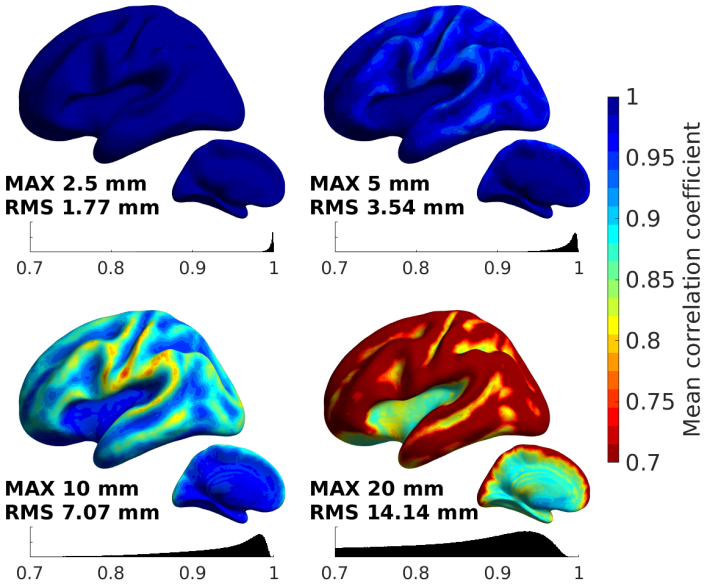

Figure 24: Average correlation coefficient (CC) of point spread functions (PSFs) over all subjects. Although only the left hemisphere is shown, the histograms include data from both hemispheres.

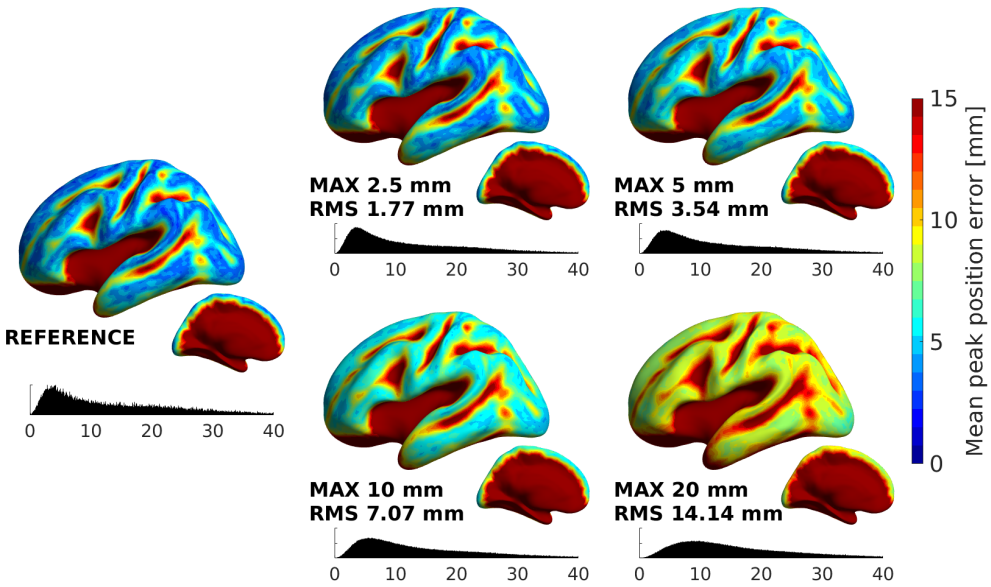

Figure 25: Average peak position error (PPE) of point spread functions (PSFs) over all subjects. Although only the left hemisphere is shown, the histograms include data from both hemispheres.

4.2.2 Beamformer simulations

The LCMV beamformer simulations echo the findings of the MNE simulations in that deep sources cannot be accurately localised regardless of sensor position error. This effect is not as pronounced as for MNE source estimation.

Without any sensor position error the mean position error of the estimated peak source power (BPE) over the simulated time interval was 0.379 mm for superficial sources and 5.7 mm for deep sources (grand average 3.2 mm). When the maximum sensor position error is 2.5 mm, the BPE grows to 0.529 mm for superficial sources and 5.8 mm for deep sources (grand average 3.4 mm). As the maximum sensor position error is increased to 5 mm, the BPE jumps to 6.4 mm for superficial sources and 6.7 mm for deep sources (grand average 6.5 mm). For even larger sensor position errors the BPEs rise quickly, especially for superficial sources, for which the BPEs become much larger than those of the deep sources (mean BPEs at 10 mm: 29.6 mm for superficial sources, 7.8 mm for deep sources and grand average 17.9 mm. Mean BPEs at 20 mm: 64.3 mm for superficial sources, 22.1 mm for deep sources and grand average 41.7 mm).

4.2.3 Dipole localisation

Looking at the dipole localisation errors in Fig. 27, many things become apparent. First of all, one can see the general effect of noise on source localisation and specifically its effect on deep sources. When no noise is included in the data (Fig. 27, top row), deep sources can actually be *more* accurately localised than shallow sources due to sensor position error. This can be explained by the smaller solid angle error between the source and the sensors due to their larger spatial separation. In a real-world scenario noise

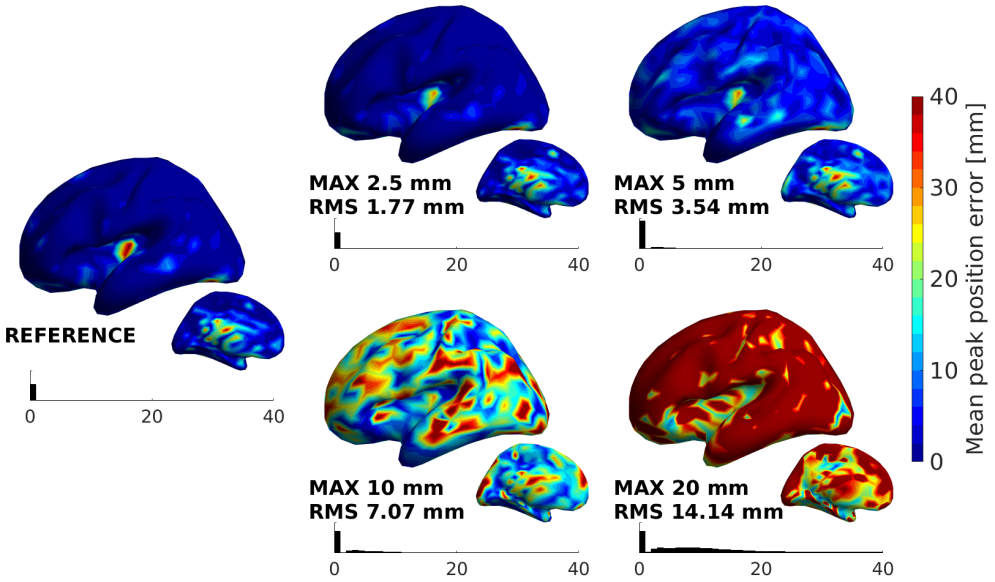

Figure 26: Average position error of the peak power in the LCMV beamformer estimate with SNR = 0.1. Although only the left hemisphere is shown, the histograms include data from both hemispheres.

is always present and thus such special cases are not relevant in practice; the results of simulations with added noise (Fig. 27, second and third rows) indicate that deep sources can be much more poorly localised than superficial sources.

Additionally, one can see that < 5-mm dipole position error is attainable (for superficial sources) when the maximum sensor position error is ≤ 5 mm, even at moderate SNR levels (Fig. 27, second column).

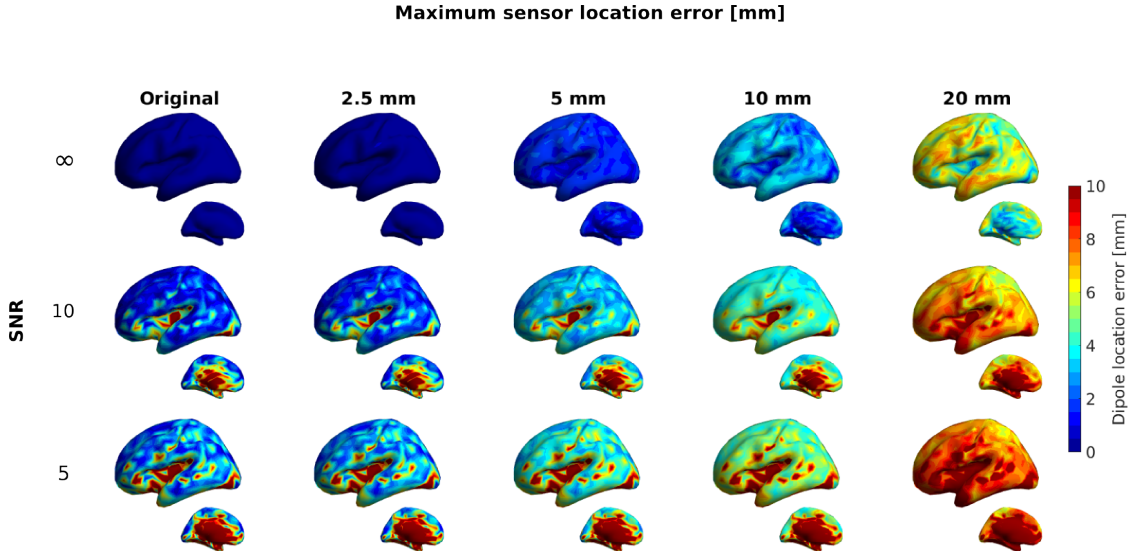

Figure 27: Average dipole localisation error over all subjects at three different SNR levels and at different maximum sensor position errors. Only the left hemisphere is shown.

Due to the large effect of noise and source depth on source localisation performance, the dipole localisation results were also visualised (Fig. 28) with sources separated into superficial and deep groups. Additionally, dipole localisation results using the 102 magnetometers of a 306-channel SQUID-based MEG system were also included as a comparison. For the SQUID-based MEG system, no sensor position error was included. For this comparison it is also important to note that the source strength and noise variance were the same for both OPM and SQUID arrays and thus the overall SNR was lower for the SQUID array due to the larger distance of the sensors from the head.

Fig. 28 again demonstrates that the dipole orientation error is *smaller* for deeper than for superficial sources when no noise is included in the simulations. The orientation error for deep sources does not increase with the sensor position error to the same degree as for superficial sources, once again due to the larger source-sensor-distances. Another important parameter in dipole fitting is the goodness-of-fit (GOF). In these simulations, the actual dipole location error is available while in real-world applications the GOF is the primary indicator of quality. Thus, GOF is widely used as an indicator of the appropriateness of any given fitted dipole, including in clinical work (see e.g. Bagić and colleagues (2011)). GOF is low (< 0.8) for deep sources in the noisy simulations regardless of sensor position error, whereas it is mostly > 0.8 for superficial sources even with sensor position errors up to 10 mm.

The results for the SQUID-based MEG system are very good when no noise is included, but deteriorate substantially when noise is added. Localisation performance of the SQUID array without any sensor position error is worse than that of the OPM array with up to 20-mm sensor position error. The poor performance is especially noticeable for deep sources, with on average larger than 45° orientation and GOF < 0.5.

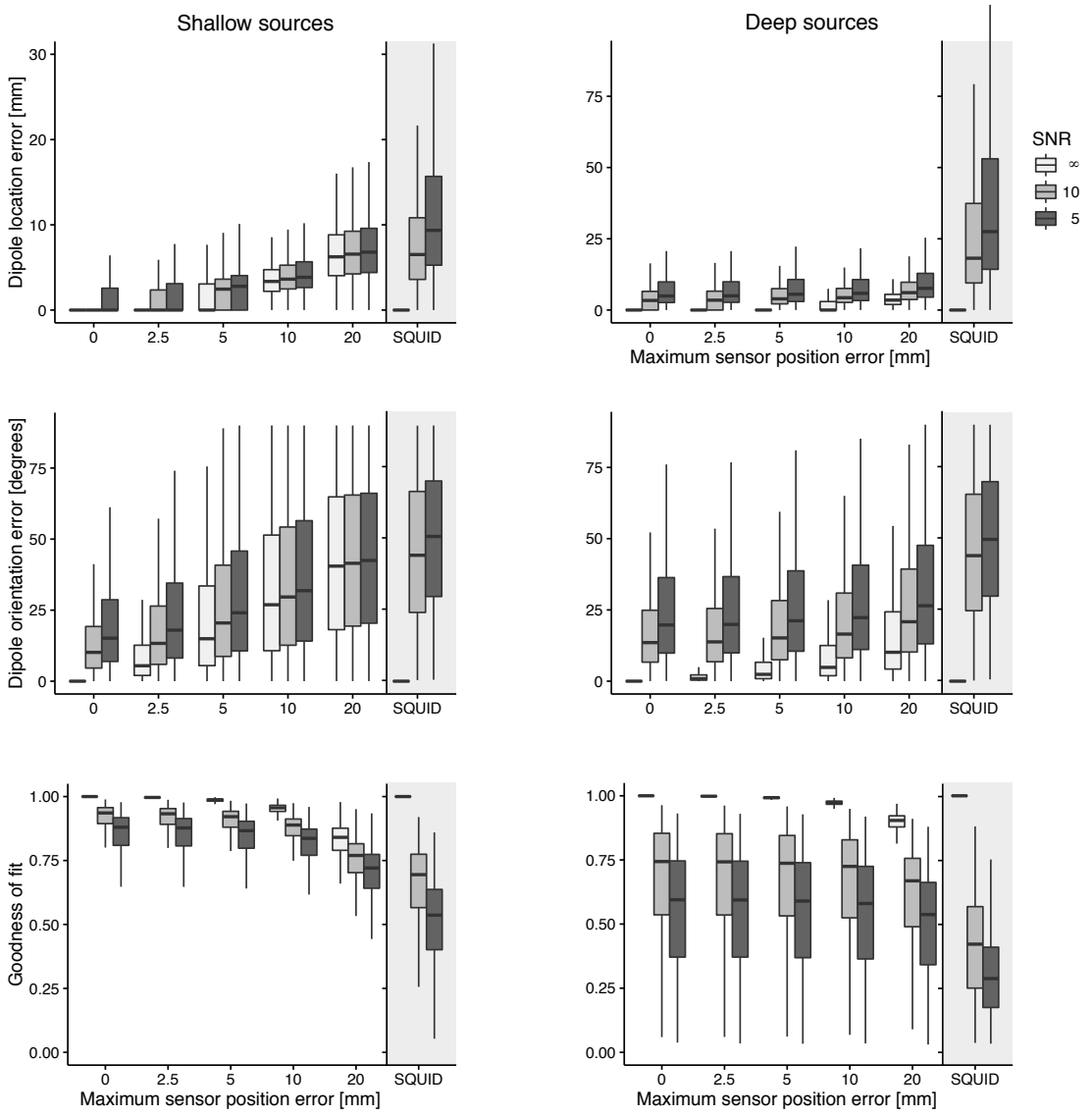

Figure 28: Dipole fitting results, including the dipole position error (top row), dipole orientation error (middle row) and goodness of fit (bottom row). The results for into shallow and deep sources are shown separately, and the results for a 102-channel SQUID magnetometer-based MEG system *without* any sensor position error are included as a comparison. The scales are not identical in all graphs.

5 Discussion

In this thesis, different co-registration methods that could be applied for on-scalp MEG were investigated from both performance and practicality perspectives. To determine the required accuracy of such a method, simulations of a hypothetical on-scalp MEG system were performed.

Simulation methodology

When interpreting the results of the simulations in this thesis, one needs to take into account the assumptions and constraints used in each simulation. For the least-squares dipole fitting procedure, different levels of noise were added to the simulations, and the orientation for the fitted dipole was kept as a free parameter. Generally speaking, one can say that dipole fitting produces quite good results for superficial sources, but is not necessarily very robust for errors in the forward model.

Due to the choice of a naïve dipole fitting algorithm, which utilises no *a priori* knowledge regarding where the dipole could reasonably be as a starting point, and the high computational load of the dipole fitting procedure for the large number of scenarios that were simulated the number of fitted dipoles was limited. Instead of simulating dipoles at every source location in the 5th-degree icosahedral space with 20484 source points, sources were picked from its subspace (a 3rd degree mesh with 1284 vertices) although the entire 5th-degree space was used for dipole fitting. Still, a grand total of 9630000 dipoles were fitted for the OPM arrays. The use of a sparse mesh explains the apparent lack of "smoothness" in Fig. 27.

The MNE simulations on the other hand were several orders of magnitude faster to compute than the dipole fitting simulations, and as such the entire 5th-degree icosahedral source space was employed. While the MNE simulations included more source locations, the constraints used were stricter. Due to the use of resolution-matrix-based metrics, no noise could be included into the simulations, and additionally sources were assumed to be oriented normally to the cortical surface. However, due to the distributed nature of minimum-norm source estimates, the orientation constraint should not affect the quality of, or the ability to interpret, the results.

The LCMV beamformer simulations include several adjustable parameters due to the nature of the method. Since the source estimate itself is determined on the basis of data covariance, an actual time course has to be constructed. The duration of this time window is of utmost importance (Brookes et al., 2008). A longer lasting time window will give a more robust estimate of the data covariance, translating into a superior source estimate assuming that the data are stationary. While the window length used in the present work was 600 samples, lengths used in previous simulation studies have been widely different, ranging from ~100 samples (Hillebrand & Barnes, 2003) to 1000 samples or even more (Boto et al., 2016). Of course, window duration is not the only consideration, as beamformer source estimation requires noise to be present in the data for the procedure to function properly. As has been observed in previous studies, too high SNR levels lead to compromised performance when using beamformers (e.g. Cox, 1973; Dalal et al., 2014). This "beamformer mismatch" could be seen as the spatial

filters being so sharp that the data from the intended pass-band is also filtered out when the forward model includes even small errors. The SNR level used for the beamformer in the present work was chosen on the basis of preliminary simulations with varied SNR levels. Here, we attempted to minimise the beamformer mismatch effect, as the main parameter of interest was the effect of sensor position error on source estimation performance.

Simulation results & implications

Based on the results of both MNE, LCMV beamformer and dipole fitting simulations, a maximum sensor location error of 5 mm (implying a RMS sensor position error of ~3.5 mm) gives rise to a source estimation error of $\lesssim 5$ mm for superficial sources. Due to the loss of SNR as the sensor-source-distance increases, errors for deep sources are much larger than for shallow sources. Due to this inherent property of MEG and the fact that most sources of interest are more or less superficial, one should concentrate on the superficial sources. Even smaller sensor position error levels result in some localisation error, albeit at a much less significant level. In the end, it is up to the user to decide how large sensor position errors can be tolerated and by extension how accurate source estimates are possible.

Out of the variety of sensor localisation methods that were examined, all seem to be accurate enough for this proposed < 5 mm error requirement. Some methods, especially the more recently developed optical ones, are more accurate than the Polhemus system but no method was utterly outclassed by the others. As such, other factors such as cost, ease of use and speed will be the deciding factors in choosing the method to be used. For example, the widely used Polhemus Fastrak system requires moving a digitiser to all channel locations, thus making the co-registration more laborious and error-prone. On the other hand, the system is proven and has wide adoption both for EEG and MEG co-registration. Optical surface mapping methods on the other hand have the potential to be fast (Koessler et al., 2011) or almost instantaneous (Bauer et al., 2000) depending on the implementation. On the other hand, when using optical methods one needs to identify the sensors non-ambiguously (see Section 2.3.1). In spite of this complication, optical surface mapping methods do seem like the most promising solution, as they can collect dense surface data, including the shape of the head and face, very quickly. This complementary information can be used in co-registration when fitting the MR image to the digitised data, providing additional benefit.

The simulations performed in this work are mainly concerning the sensor *position* error, although the sensor *orientation* error also affects results in a similar manner. Orientation error was not included in the simulations as to limit the number of variables under examination and keep the computational workload within reasonable limits.

Other sources of error

Sensor localisation is just one part of the co-registration process, and thus is not the only source of co-registration error. Once the position and orientation of the sensors and the fiducials are known in a common coordinate system, the fiducials are fitted to the MR

images as discussed in Section 2.1.5. A variety of algorithms for this fitting procedure exist. Fitting techniques solely using the fiducial locations are generally considered inferior to those that additionally use denser surface data.

As implied by the results of the simulations including other sources of error, namely noise, co-registration error is only one part of the equation. Other significant types of errors in the forward solution include model errors such as geometric errors in the BEM meshes and errors in conductivity.

For example, an error in the skull conductivity of ~60% gives rise to a relative lead field error (RE) of 11%, while a maximum sensor position error of 5 mm (RMS error 3.54 mm) causes an RE of 12.24% (Stenroos & Hauk, 2013). Generally speaking, the forward model is not all too sensitive to the resistivity ratio of the skull: it can be over- or underestimated by a ratio of 1.5 without causing RE of > 1% (Stenroos & Nummenmaa, 2016). The previous comparison does not take into account the effect of the CSF, whose omission in the head model can result in an RE of ~20% when compared to a model including the CSF (Stenroos & Nummenmaa, 2016).

Geometric errors in the boundary element meshes may occur due to incorrect segmentation of MR images. Incorrect segmentation can occur both due to the use of automatic segmentation algorithms (Stenroos et al., 2014) as well as artifacts and low SNR levels present in the MR image.

Prospects

At the time of writing, several research groups have developed OPMs that can be and have been applied to MEG both in humans (Shah & Wakai, 2013) and animals (Alem et al., 2014). The sensors and experimental set-ups vary from single-channel measurements using physically very large magnetometers (Xia et al., 2006; Kamada et al., 2015) to microfabricated sensors (Shah & Wakai, 2013; Knappe et al., 2014) that could feasibly be deployed in a sensor array covering the entire scalp (Fig. 15). Even though sensors applicable for a whole-head sensor array with a large number of channels have been developed, no such system has been demonstrated at the time of writing of this thesis. Remaining challenges, apart from co-registration, include shielding and cross-talk issues as well as cost reduction.

Another remaining challenge tangentially related to co-registration is the matter of how to support the OPM sensor array upon the heads of subjects. The optimal solution would be to use a head cap like in EEG, but it remains to be seen if such a solution provides enough support for the OPMs, which are substantially heavier and larger than EEG electrodes.

Despite these challenges, on-scalp MEG based on OPMs has enormous potential to rejuvenate the field of MEG and to provide a better neuroimaging tool for neuroscientists and clinicians alike.

6 Conclusions

In this thesis, different methods for accurately determining the position of sensors in on-scalp MEG were examined, whereafter simulations were performed to determine the maximum acceptable sensor position error. Through the use of several performance metrics and simulations, the maximum acceptable RMS sensor position error in on-scalp MEG was found to be ~3 mm although smaller levels of error do provide additional benefit. Most methods examined in this thesis were able to reach this maximum acceptable error level. Depending on the application, the choice of method for determining the sensor positions may depend not only on performance but also on other factors such as cost, ease of use and commercial availability.

References

3D-Shape GmbH. FaceSCAN3D. Online: http://www.3d-shape.com/produkte/face_e.php.

Adjamian, P, G. R Barnes, A Hillebrand, I. E Holliday, K. D Singh, P. L Furlong, E Harrington, C. W Barclay and P. J. G Route. 2004. Co-registration of magnetoencephalography with magnetic resonance imaging using bite-bar-based fiducials and surface-matching. *Clinical Neurophysiology* 115:691–698.

Ahlfors, S and R. J Ilmoniemi. 1989. Magnetometer position indicator for multichannel MEG. *Advances in Biomagnetism*, 693–696. Springer.

Akhtari, M, H. C Bryant, A. N Mamelak, E. R Flynn, L Heller, J. J Shih, M Mandelkern, A Matlachov, D. M Ranken, E. D Best, M. A DiMauro, R. R Lee and W. W Sutherling. 2002. Conductivities of three-layer live human skull. *Brain Topography* 14:151–167.

Alem, O, A. M Benison, D. S Barth, J Kitching and S Knappe. 2014. Magnetoencephalography of epilepsy with a microfabricated atomic magnetrode. *Journal of Neuroscience* 34:14324–14327.

Artec Group Inc. Artec Eva 3D Object Scanner. Online: https://www.artec3d.com/artec-eva#specifications.

Asztalos, S. J, G Carosi, C Hagmann, D Kinion, K Van Bibber, M Hotz, L. J Rosenberg, G Rybka, J Hoskins, J Hwang, P Sikivie, D. B Tanner, R Bradley and J Clarke. 2010. SQUID-based microwave cavity search for dark-matter axions. *Physical Review Letters* 104:041301.

Auzinsh, M, D Budker, D. F Kimball, S. M Rochester, J. E Stalnaker, A. O Sushkov and V. V Yashchuk. 2004. Can a Quantum Nondemolition Measurement Improve the Sensitivity of an Atomic Magnetometer? *Physical Review Letters* 93:173002.

Bagić, A. I, R. C Knowlton, D. F Rose and J. S Ebersole. 2011. American Clinical Magnetoencephalography Society Clinical Practice Guideline 1: recording and analysis of spontaneous cerebral activity. *Journal of Clinical Neurophysiology* 28:348–354.

Baillet, S. 2010. The Dowser in the Fields: Searching for MEG Sources. *MEG: An Introduction to Methods*, ed. by P Hansen, M Kringelbach, and R Salmelin, Chap. 5. Oxford University Press.

Balabas, M. V, T Karaulanov, M. P Ledbetter and D Budker. 2010. Polarized Alkali-Metal Vapor with Minute-Long Transverse Spin-Relaxation Time. *Physical Review Letters* 105:070801.

Bardeen, J, L Cooper and J Schrieffer. 1957. Theory of superconductivity. *Physical Review* 108:1175.

Barone, A and G Paterno. 1982. *Physics and applications of the Josephson effect*. John Wiley & Sons.

Battistelli, E. S, M Amiri, B Burger, M Halpern, S Knotek, M Ellis, X Gao, D Kelly, M MacIntosh, K Irwin and C Reintsema. 2008. Functional description of read-out electronics for time-domain multiplexed bolometers for millimeter and sub-millimeter astronomy. *Journal of Low Temperature Physics* 151:908–914.

Bauer, H, C Lamm, S Holzreiter, I Holländer, U Leodolter and M Leodolter. 2000. Measurement of 3D electrode coordinates by means of a 3D photogrammetric head digitizer. *NeuroImage* 11:S461.

Baysal, U and G Şengül. 2010. Single Camera photogrammetry system for EEG electrode identification and localization. *Annals of Biomedical Engineering* 38:1539–1547.

Boto, E, R Bowtell, P Kruger, M. T Fromhold, P. G Morris, S. S Meyer, G. R Barnes and M. J Brookes. 2016. On the Potential of a new generation of Magnetometers for MEG: a Beamformer Simulation Study. *PLoS ONE* 11:1–24.

Bouchiat, M. A and J Brossel. 1966. Relaxation of optically pumped Rb atoms on paraffin-coated walls. *Physical Review* 147:41–54.

Brebbia, C. A, J. C. F Telles and L Wrobel. 2012. *Boundary element techniques: theory and applications in engineering*. Springer Science & Business Media.

Brinkmann, B. H, T. J O'Brien, M. A Dresner, T. D Lagerlund, F. W Sharbrough and R. A Robb. 1998. Scalp-recorded EEG localization in MRI volume data. *Brain Topography* 10:245–253.

Brookes, M. J, J Vrba, S. E Robinson, C. M Stevenson, A. M Peters, G. R Barnes, A Hillebrand and P. G Morris. 2008. Optimising experimental design for MEG beamformer imaging. *NeuroImage* 39:1788–1802.

Brossel, J, J Margerie and A Kastler. 1955. Augmentation du taux d'orientation atomique de la vapeur de Sodium en presence d'Hydrogene. *Comptes rendus hebdomadaires des séances de l'Académie* 241:865–867.

Budker, D and D. F. J Kimball. 2013. *Optical Magnetometry*. Cambridge University Press.

Budker, D and M Romalis. 2007. Optical magnetometry. *Nature Physics* 3:227–234.

Carlson, N. R. 1992. *Foundations of physiological psychology*. 2nd edn. Allyn and Bacon.

Carrette, E, M Op De Beeck, M Bourguignon, P Boon, K Vonck, B Legros, S Goldman, P Van Bogaert and X De Tiege. 2011. Recording temporal lobe epileptic activity with MEG in a light-weight magnetic shield. *Seizure* 20:414–418.

Cohen, D. 1968. Magnetoencephalography: Evidence of magnetic fields produced by alpha-rhythm currents. *Science* 161:784–786.

Cohen, D. 1972. Magnetoencephalography: Detection of the brain's electrical activity with a superconducting magnetometer. *Science* 175:664–666.

Cox, H. 1973. Resolving power and sensitivity to mismatch of optimum array processors. *Journal of the Acoustical Society of America* 54:771–785.

Creaform Inc. 2015. HandySCAN 3D™. Online: http://www.creaform3d.com/sites/default/files/assets/brochures/files/handyscan/2016/handyscan3d_brochure_en_hq_21032016.pdf.

Dalal, S. S, S Rampp, F Willomitzer and S Ettl. 2014. Consequences of EEG electrode position error on ultimate beamformer source reconstruction performance. *Frontiers in Neuroscience* 8:42.

Dale, A. M, B Fischl and M. I Sereno. 1999. Cortical surface-based analysis. I. Segmentation and surface reconstruction. *NeuroImage* 9:179–194.

Dannhauer, M, B Lanfer, C. H Wolters and T. R Knösche. 2011. Modeling of the human skull in EEG source analysis. *Human Brain Mapping* 32:1383–1399.

De Munck, J. C, P. C. M Vijn and H Spekreijse. 1991. A practical method for determining electrode positions on the head. *Electroencephalography and Clinical Neurophysiology* 78:85–87.

Ettl, S. 2015. Introductory review on 'Flying Triangulation': a motion-robust optical 3D measurement principle. *Contemporary Physics* 56:144–158.

Ettl, S, O Arold, Z Yang and G Häusler. 2012. Flying triangulation—an optical 3D sensor for the motion-robust acquisition of complex objects. *Applied Optics* 51:281–289.

Ettl, S, S Rampp, S Fouladi-Movahed, S. S Dalal, F Willomitzer, O Arold, H Stefan and G Häusler. 2013. Improved EEG source localization employing 3D sensing by "Flying Triangulation". *SPIE Optical Metrology 2013* 87910V.

Ferguson, A. S and G Stroink. 1997. Factors affecting the accuracy of the boundary element method in the forward problem-I: Calculating surface potentials. *IEEE Transactions on Biomedical Engineering* 44:1139–1155.

Fischl, B. 2012. FreeSurfer. *NeuroImage* 62:774–781.

Fischl, B, M. I Sereno and A. M Dale. 1999a. Cortical Surface-Based Analysis II: Inflation, Flattening, and a Surface-Based Coordinate System. *NeuroImage* 9:195–207.

Fischl, B, M. I Sereno, R. B. H Tootell and A. M Dale. 1999b. High-resolution intersubject averaging and a coordinate system for the cortical surface. *Human Brain Mapping* 8:272–284.

Fleischhauer, M, A. B Matsko and M. O Scully. 2000. Quantum limit of optical magnetometry in the presence of ac-Stark shifts. *Physical Review A* 62:11.

George, J. S, P. S Jackson, D. M Ranken and E. R Flynn. 1989. Three-dimensional volumetric reconstruction for neuromagnetic source localization. *Advances in Biomagnetism*, ed. by S. J Williamson, M Hoke, G Stroink, and M Kotani, pp. 737–740. Springer US.

Geselowitz, D. B. 1970. On the Magnetic Field Generated Outside an Inhomogeneous Volume Conductor by Internal Current Sources. *IEEE Transactions on Magnetics* 6:346–347.

Goldenholz, D. M, S. P Ahlfors, M. S Hämäläinen, D Sharon, M Ishitobi, L. M Vaina and S. M Stufflebeam. 2009. Mapping the signal-to-noise-ratios of cortical sources in magnetoencephalography and electroencephalography. *Human Brain Mapping* 30:1077–1086.

Gramfort, A, M Luessi, E Larson, D. A Engemann, D Strohmeier, C Brodbeck, L Parkkonen and M. S Hämäläinen. 2014. MNE software for processing MEG and EEG data. *NeuroImage* 86:446–460.

Grave De Peralta Menendez, R, O Hauk, S. G Andino, H Vogt and C Michel. 1997. Linear inverse solutions with optimal resolution kernels applied to electromagnetic tomography. *Human Brain Mapping* 5:454–467.

Hämäläinen, M. S, R Hari, R. J Ilmoniemi, J Knuutila and O. V Lounasmaa. 1993. Magnetoencephalography—theory, instrumentation, and applications to noninvasive studies of the working human brain. *Reviews of Modern Physics* 65:413–505.

Happer, W. 1972. Optical Pumping. *Reviews of Modern Physics* 44:169–250.

Happer, W and B. S Mathur. 1967. Effective operator formalism in optical pumping. *Physical Review* 163:12–25.

Happer, W and A. C Tam. 1977. Effect of rapid spin exchange on the magnetic-resonance spectrum of alkali vapors. *Physical Review A* 16:1877–1891.

Happer, W and H Tang. 1973. Spin-exchange shift and narrowing of magnetic resonance lines in optically pumped alkali vapors. *Physical Review Letters* 31:273–276.

Haueisen, J, C Ramon, M Eiselt, H Brauer and H Nowak. 1997. Influence of tissue resistivities on neuromagnetic fields and electric potentials studied with a finite element model of the head. *IEEE Transactions on Biomedical Engineering* 44:727–735.

Hauk, O, D. G Wakeman and R Henson. 2011. Comparison of noise-normalized minimum norm estimates for MEG analysis using multiple resolution metrics. *NeuroImage* 54:1966–1974.

Hillebrand, A and G. R Barnes. 2003. The use of anatomical constraints with MEG beamformers. *NeuroImage* 20:2302–2313.

Hillebrand, A and G. R Barnes. 2005. Beamformer Analysis of MEG Data. *International Review of Neurobiology* 68:149–171.

Hillebrand, A and G. R Barnes. 2011. Practical constraints on estimation of source extent with MEG beamformers. *NeuroImage* 54:2732–2740.

Hironaga, N, K Hagiwara, K Ogata, M Hayamizu, T Urakawa and S Tobimatsu. 2014. Proposal for a new MEG–MRI co-registration: A 3D laser scanner system. *Clinical Neurophysiology* 125:2404–2412.

Huang, M. X, J. J Shih, R. R Lee, D. L Harrington, R. J Thoma, M. P Weisend, F Hanlon, K. M Paulson, T Li, K Martin, G. A Miller and J. M Canive. 2004. Commonalities and Differences among Vectorized Beamformers in Electromagnetic Source Imaging. *Brain Topography* 16:139–158.

Huppertz, H.-J, M Otte, C Grimm, R Kristeva-Feige, T Mergner and C. H Lücking. 1998. Estimation of the accuracy of a surface matching technique for registration of EEG and MRI data. *Electroencephalography and Clinical Neurophysiology* 106:409–415.

Iivanainen, J. 2016. *Active magnetic shield for optical neuromagnetic measurements*. M.Sc. thesis, Aalto University.

Jaklevic, R. C, J Lambe, A. H Silver and J. E Mercereau. 1964. Quantum interference effects in Josephson tunneling. *Physical Review Letters* 12:159–160.

Jasper, H. H. 1958. The ten-twenty electrode system of the International Federation. *Electroencephalography and Clinical Neurophysiology* 10:371–375.

Johnson, C and P. D. D Schwindt. 2010. A two-color pump probe atomic magnetometer for magnetoencephalography. *2010 IEEE International Frequency Control Symposium, FCS 2010*, pp. 371–375.

Johnson, C. N, P. D. D Schwindt and M Weisend. 2013. Multi-sensor magnetoencephalography with atomic magnetometers. *Physics in Medicine and Biology* 58:6065–6077.

Josephson, B. 1962. Possible new effects in superconductive tunnelling. *Physics Letters* 1:251–253.

Kamada, K, D Sato, Y Ito, H Natsukawa, K Okano, N Mizutani and T Kobayashi. 2015. Human magnetoencephalogram measurements using newly developed compact module of high-sensitivity atomic magnetometer. *Japanese Journal of Applied Physics* 54:026601.

Khosla, D, M Don and B Kwong. 1999. Spatial mislocalization of EEG electrodes - Effects on accuracy of dipole estimation. *Clinical Neurophysiology* 110:261–271.

Kim, K, S Begus, H Xia, S.-K Lee, V Jazbinsek, Z Trontelj and M. V Romalis. 2014. Multi-channel atomic magnetometer for magnetoencephalography: a configuration study. *NeuroImage* 89:143–51.

Kim, S. G, W Richter and K Ugurbil. 1997. Limitations of temporal resolution in functional MRI. *Magnetic Resonance in Medicine* 37:631–636.

Kimball, D. F. J, E. B Alexandrov and D Budker. 2013. General principles and characteristics of optical magnetometers. *Optical magnetometry*, ed. by D Budker and D. F Jackson Kimball, Chap. 1. Cambridge University Press.

Knappe, S, T Sander and L Trahms. 2014. Optically-Pumped Magnetometers for MEG. *Magnetoencephalography: From signals to dynamic cortical networks*, pp. 993–999. Springer Berlin Heidelberg.

Koessler, L, T Cecchin, O Caspary, A Benhadid, H Vespignani and L Maillard. 2011. EEG-MRI co-registration and sensor labeling using a 3D laser scanner. *Annals of Biomedical Engineering* 39:983–995.

Koessler, L, T Cecchin, E Ternisien and L Maillard. 2010. 3D handheld laser scanner based approach for automatic identification and localization of EEG sensors. *2010 Annual International Conference of the IEEE Engineering in Medicine and Biology Society, EMBC'10*, pp. 3707–3710.

Koessler, L, L Maillard, A Benhadid, J. P Vignal, M Braun and H Vespignani. 2007. Spatial localization of EEG electrodes. *Neurophysiologie Clinique* 37:97–102.

Kominis, I. K, T. W Kornack, J. C Allred and M. V Romalis. 2003. A subfemtotesla multichannel atomic magnetometer. *Nature* 422:596–599.

Lai, Y, W Van Drongelen, L Ding, K. E Hecox, V. L Towle, D. M Frim and B He. 2005. Estimation of in vivo human brain-to-skull conductivity ratio from simultaneous extra- and intra-cranial electrical potential recordings. *Clinical Neurophysiology* 116:456–465.

Lamm, C, C Windischberger, U Leodolter, E Moser and H Bauer. 2001. Co-registration of EEG and MRI data using matching of spline interpolated and MRI-segmented reconstructions of the scalp surface. *Brain Topography* 14:93–100.

Le, J, M Lu, E Pellouchoud and A Gevins. 1998. A rapid method for determining standard 10/10 electrode positions for high resolution EEG studies. *Electroencephalography and Clinical Neurophysiology* 106:554–558.

Ledbetter, M. P, I. M Savukov, V. M Acosta, D Budker and M. V Romalis. 2008. Spin-exchange-relaxation-free magnetometry with Cs vapor. *Physical Review A* 77:1–7.

Lee, Y.-H and K Kim. 2014. Instrumentation for Measuring MEG Signals. *Magnetoencephalography: From signals to dynamic cortical networks*, ed. by S Supek and C. J Aine, pp. 3–33. Springer Berlin Heidelberg.

Lin, F. H, T Witzel, S. P Ahlfors, S. M Stufflebeam, J. W Belliveau and M. S Hämäläinen. 2006. Assessing and improving the spatial accuracy in MEG source localization by depth-weighted minimum-norm estimates. *NeuroImage* 31:160–171.

Lopes da Silva, F. H. 2010. Electrophysiological Basis of MEG Signals. *Meg: An introduction to methods*, ed. by P Hansen, M Kringelbach, and R Salmelin, Chap. 1. Oxford University Press.

Michel, C. M, M. M Murray, G Lantz, S Gonzalez, L Spinelli and R Grave De Peralta. 2004. EEG source imaging. *Clinical Neurophysiology* 115:2195–2222.

Murakami, S and Y Okada. 2006. Contributions of principal neocortical neurons to magnetoencephalography and electroencephalography signals. *Journal of Physiology* 575:925–936.

Nenonen, J, J Nurminen, D Kičić, R Bikmullina, P Lioumis, V Jousmäki, S Taulu, L Parkkonen, M Putaala and S Kähkönen. 2012. Validation of head movement correction and spatiotemporal signal space separation in magnetoencephalography. *Clinical Neurophysiology* 123:2180–2191.

Oostendorp, T. F, J Delbeke and D. F Stegeman. 2000. The conductivity of the human skull: Results of *in vivo* and *in vitro* measurements. *IEEE Transactions on Biomedical Engineering* 47:1487–1492.

Parkkonen, L. 2009. *Expanding the applicability of Magnetoencephalography*. Helsinki Unversity of Technology Dissertation.

Parkkonen, L. 2010. Instrumentation and Data Preprocessing. *MEG: An Introduction to Methods*, ed. by P Hansen, M Kringelbach, and R Salmelin, Chap. 2. Oxford University Press.

Polhemus Incorporated. 2012. Polhemus FASTRAK Broschure. Online: `http://polhemus.com/_assets/img/FASTRAK_Brochure.pdf`.

Preusser, J, V Gerginov, S Knappe and J Kitching. 2008. A microfabricated photonic magnetometer. *Proceedings of the Seventh IEEE Sensors Conference*, pp. 344–346.

Qian, S and Y Sheng. 2011. A Single Camera Photogrammetry System for Multi-angle Fast Localization of EEG Electrodes. *Annals of Biomedical Engineering* 39:2844–2856.

Russell, G. S, K. J Eriksen, P Poolman, P Luu and D. M Tucker. 2005. Geodesic photogrammetry for localizing sensor positions in dense-array *EEG*. *Clinical Neurophysiology* 116:1130–1140.

Sai Siva Gorthi, P. R. 2010. Fringe Projection Techniques: Whither we are? *Optics and Lasers in Engineering* 48:133–140.

Salmelin, R. 2010. Multi-Dipole Modeling in MEG. *MEG: An Introduction to Methods*, ed. by P Hansen, M Kringelbach, and R Salmelin, Chap. 6. Oxford University Press.

Sarvas, J. 1987. Basic mathematical and electromagnetic concepts of the biomagnetic inverse problem. *Physics in medicine and biology* 32:11–22.

Savukov, I and S. J Seltzer. 2013. Spin-exchange-relaxation-free (SERF) magnetometers. *Optical magnetometry*, ed. by D Budker and D. F Jackson Kimball, Chap. 5. Cambridge University Press.

Schmidt, P, D Clark, K Leslie, M Bick, D Tilbrook and C Foley. 2004. GETMAG–A SQUID magnetic tensor gradiometer for mineral and oil exploration. *Exploration Geophysics* 35:297.

Ségonne, F, A. M Dale, E Busa, M Glessner, D Salat, H. K Hahn and B Fischl. 2004. A hybrid approach to the skull stripping problem in MRI. *NeuroImage* 22:1060–1075.

Sekihara, K, S. S Nagarajan, D Poeppel and A Marantz. 2004. Performance of an MEG Adaptive-Beamformer Source Reconstruction Technique in the Presence of Additive Low-Rank Interference. *IEEE Transactions on Biomedical Engineering* 51:90–99.

Seltzer, S. J. 2008. *Developments in Alkali-Metal Atomic Magnetometry*. Princeton University dissertation.

Seltzer, S. J and M. V Romalis. 2004. Unshielded three-axis vector operation of a spin-exchange-relaxation-free atomic magnetometer. *Applied Physics Letters* 85:4804–4806.

Shah, V and M. V Romalis. 2009. Spin-exchange relaxation-free magnetometry using elliptically polarized light. *Physical Review A* 80:1–6.

Shah, V. K and R. T Wakai. 2013. A compact, high performance atomic magnetometer for biomedical applications. *Physics in Medicine and Biology* 58:8153–8161.

Song, J, C Davey, C Poulsen, P Luu, S Turovets, E Anderson, K Li and D Tucker. 2015. EEG source localization: Sensor density and head surface coverage. *Journal of Neuroscience Methods* 256:9–21.

Srinivasan, V, H. C Liu and M Halioua. 1984. Automated phase-measuring profilometry of 3-D diffuse objects. *Applied Optics* 23:3105–3108.

Stenroos, M and O Hauk. 2013. Minimum-norm cortical source estimation in layered head models is robust against skull conductivity error. *NeuroImage* 81:265–272.

Stenroos, M, A Hunold and J Haueisen. 2014. Comparison of three-shell and simplified volume conductor models in magnetoencephalography. *NeuroImage* 94:337–348.

Stenroos, M and A Nummenmaa. 2016. Incorporating and Compensating Cerebrospinal Fluid in Surface-Based Forward Models of Magneto- and Electroencephalography. *PLOS ONE* 11:e0159595.

Stenroos, M and J Sarvas. 2012. Bioelectromagnetic forward problem: isolated source approach revis(it)ed. *Physics in Medicine and Biology* 57:3517–3535.

Szabo, B. A and I Babuška. 1991. *Finite element analysis*. John Wiley & Sons.

Towle, V. L, J Bolaños, D Suarez, K Tan, R Grzeszczuk, D. N Levin, R Cakmur, S. A Frank and J. P Spire. 1993. The spatial location of EEG electrodes: locating the best-fitting sphere relative to cortical anatomy. *Electroencephalography and Clinical Neurophysiology* 86:1–6.

Tripp, J. 1981. Biomagnetic fields and cellular current flow. *Biomagnetism*, ed. by S Erné, H Hahlbohm, and H Lübbig, pp. 207–215. Walter de Gruyter.

Troebinger, L, J. D López, A Lutti, D Bradbury, S Bestmann and G Barnes. 2014. High precision anatomy for MEG. *NeuroImage* 86:583–591.

Van Veen, B, W van Drongelen, M Yuchtman and A Suzuki. 1997. Localization of brain electrical activity via linearly constrained minimum variance spatial filtering. *IEEE Transactions on Biomedical engineering* 44:867–880.

Vrba, J, S Taulu, J Nenonen and A Ahonen. 2010. Signal space separation beamformer. *Brain Topography* 23:128–133.

Wang, Y and J Gotman. 2001. The influence of electrode location errors on EEG dipole source localization with a realistic head model. *Clinical Neurophysiology* 112:1777–1780.

Whalen, C, E. L Maclin, M Fabiani and G Gratton. 2008. Validation of a method for coregistering scalp recording locations with 3D structural MR images. *Human Brain Mapping* 29:1288–1301.

Williamson, S. J and L Kaufman. 1989. Advances in neuromagnetic instrumentation and studies of spontaneous brain activity. *Brain Topography* 2:129–139.

Wolters, C. H, A Anwander, X Tricoche, D Weinstein, M. A Koch and R. S MacLeod. 2006. Influence of tissue conductivity anisotropy on EEG/MEG field and return current computation in a realistic head model: A simulation and visualization study using high-resolution finite element modeling. *NeuroImage* 30:813–826.

Wong, K. V and A Hernandez. 2012. A Review of Additive Manufacturing. *ISRN Mechanical Engineering* 2012:1–10.

Wyllie, R, M Kauer, G. S Smetana, R. T Wakai and T. G Walker. 2012a. Magnetocardiography with a modular spin-exchange relaxation-free atomic magnetometer array. *Physics in Medicine and Biology* 57:2619–2632.

Wyllie, R, M Kauer, R. T Wakai and T. G Walker. 2012b. Optical magnetometer array for fetal magnetocardiography. *Optics letters* 37:2247–2249.

Xia, H, A Ben-Amar Baranga, D Hoffman and M. V Romalis. 2006. Magnetoencephalography with an atomic magnetometer. *Applied Physics Letters* 89:211104.

zebris Medical GmbH. 2005. zebris ELPOS Broschure. Online: `http://www.zebris.de/english/pdf/e_Elguide_l.pdf`.

Zhang, Y, W Van Drongelen and B He. 2006. Estimation of in vivo brain-to-skull conductivity ratio in humans. *Applied Physics Letters* 89:223903.